

High-resolution Navier-Stokes simulations of Richtmyer-Meshkov instability with re-shock

Man Long Wong*

*Department of Aeronautics and Astronautics, Stanford University
Stanford, CA 94305, USA*

Daniel Livescu†

*CCS-2, Los Alamos National Laboratory
Los Alamos, NM 87545, USA*

Sanjiva K. Lele‡

*Department of Aeronautics and Astronautics &
Department of Mechanical Engineering, Stanford University
Stanford, CA 94305, USA*

(Dated: June 14, 2022)

The interaction of a Mach 1.45 shock wave with a perturbed planar interface between sulphur hexafluoride and air is studied through high-resolution two-dimensional (2D) and three-dimensional (3D) shock-capturing adaptive mesh refinement simulations of multi-species Navier-Stokes equations. The sensitivities of time-dependent statistics on grid resolution for 2D and 3D simulations are evaluated to ensure the accuracy of the results. The numerical results are used to examine the differences between the development of 2D and 3D Richtmyer-Meshkov instability during two different stages: (1) initial growth of hydrodynamic instability from multi-mode perturbations after first shock and (2) transition to chaotic or turbulent state after re-shock. The effects of the Reynolds number on the mixing in 3D simulations are also studied through varying the transport coefficients.

arXiv:1812.01785v1 [physics.flu-dyn] 5 Dec 2018

* wongml@stanford.edu

† livescu@lanl.gov

‡ lele@stanford.edu

I. INTRODUCTION

Richtmyer-Meshkov (RM) instability, or RMI [1, 2], is a fundamental hydrodynamic flow instability that occurs when a shock wave passes through a material interface between fluids of different densities. The instability is initiated by the deposition of vorticity at the interface due to the misalignment in the pressure and density gradients across the shock wave and material interface. Studying RMI is very important for understanding the dynamics of supernovae and other astrophysical explosions, mixing enhancement in supersonic/hypersonic combustion, and turbulence and mixing limitations for inertial confinement fusion.

The study of RMI through physical experiments is challenging because the flows are transient, the initial conditions of the interface are difficult to be characterized, and uncertainty-quantified measurements are hard to be obtained. The initial perturbation grows nonlinearly soon after the passage of the shock through the interface. The growth of the mixing region is known to be largely dependent on the characteristics of initial perturbation and hence a precise control of the initial conditions is required from experiments. If the Reynolds number is sufficiently high, small-scale turbulent features will develop beyond the mixing transition. Characterizing the turbulent mixing requires high-resolution temporal and spatial measurements of both the density and velocity fields. The simultaneous planar laser-induced fluorescence (PLIF) and particle image velocimetry (PIV) measurements have been used to collect density and velocity data from shock-induced mixing problems in many previous studies [3–7]. However, the method is only limited to the measurements of the fields in a two-dimensional plane and data of other important quantities such as pressure and temperature are still out of reach. As a consequence, numerical simulations are commonly used as a complement to study the turbulent mixing induced by RMI.

As this moment, direct numerical simulation (DNS) of turbulent mixing from RMI is still computationally too expensive. However, many high-fidelity simulations and large eddy simulations (LES's) have been conducted in the past to study the development of turbulent mixing from RMI. Thornber *et al.* [8] showed the strong influence on the growth of instability from perturbations with different bandwidths using shock-capturing simulations. Hill *et al.* [9] performed LES's of RMI with re-shock using hybrid shock-capturing/bandwidth optimized centre-difference scheme with stretched-vortex subgrid-scale model in an adaptive mesh refinement framework and their results showed good agreement with experimental data. Lombardini *et al.* [10] later used the same numerical method to examine the Atwood number dependence of RMI, followed by a Mach number dependence study [11]. The uncertainty of turbulence statistics in under-resolved simulations of RMI was later explored by Tritschler *et al.* [12] for different numerical methods. While all studies mentioned above focused on the baroclinic instability in planar geometry, there are also some studies of the instabilities with inclined [13] and spherical interfaces [14, 15].

Although typical applications of shock-driven turbulent mixing require the multi-component governing equations to be solved in three-dimensional (3D) domains, one may still desire to conduct two-dimensional (2D) simulations to characterize the dynamics in the nonlinear pre-turbulent regime and take advantage of the lower requirement on computational resources. Before the onset of fully developed turbulence and especially during the initial growth of the shock-induced instability, there may be similarities in the development of the instability between 2D and 3D configurations. Olson and Greenough [16] compared the 2D and 3D simulations of RMI using the artificial fluid LES method but the mixing statistics obtained from their highest resolution simulations are still very grid-sensitive. Thornber and Zhou [17] also studied the 2D RMI with up to 64 realizations of inviscid simulations to reduce the statistical variability of their results but they did not study the effect of re-shock on the 2D instability. In this paper, we have conducted a large number of realizations of high-resolution Navier-Stokes simulations of 2D RMI with re-shock to investigate the difference between 2D and 3D RMI induced mixing.

In many previous RMI studies [8, 18, 19], the hydrodynamic equations were solved without the molecular viscous and diffusive terms. The argument for not including these terms is that the physical dissipation or diffusion can be represented by numerical dissipation or diffusion, by assuming that there is only forward cascade of energy from large scale to small scale features. While this might be relevant during the decay of the fully turbulent mixing region, the molecular transport terms could have a strong effect on the initial growth of mixing layer before mixing transition occurs. In this work, we have chosen the initial conditions for the 3D simulations such that the flows inside the mixing layers have not transitioned to turbulence yet before re-shock. By varying the transport coefficients, multiple cases with effectively different turbulent Reynolds numbers have been conducted to study the diffusive and viscous effects on the shock-driven mixing before and after re-shock.

II. GOVERNING EQUATIONS

The equations solved in this study are the conservative multi-component Navier-Stokes equations:

$$\frac{\partial \rho Y_i}{\partial t} + \nabla \cdot (\rho \mathbf{u} Y_i) + \nabla \cdot \mathbf{J}_i = 0, \quad (1)$$

$$\frac{\partial \rho \mathbf{u}}{\partial t} + \nabla \cdot (\rho \mathbf{u} \mathbf{u} + p \boldsymbol{\delta}) - \nabla \cdot \boldsymbol{\tau} = 0, \quad (2)$$

$$\frac{\partial E}{\partial t} + \nabla \cdot [(E + p) \mathbf{u}] - \nabla \cdot (\boldsymbol{\tau} \cdot \mathbf{u} - \mathbf{q}_c - \mathbf{q}_d) = 0, \quad (3)$$

where ρ , $\mathbf{u} = [u, v, w]^T = [u_1, u_2, u_3]^T$, p , and E are the density, velocity vector, pressure, and total energy per unit volume of the fluid mixture, respectively. Y_i is the mass fraction of species $i \in [1, 2, \dots, N]$, with N the total number of species. All Y_i 's sum up to one by definition. \mathbf{J}_i is diffusive mass flux for species i . $\boldsymbol{\tau}$, \mathbf{q}_c , and \mathbf{q}_d are viscous stress tensor, conductive heat flux, and inter-species diffusional enthalpy flux, respectively. $\boldsymbol{\delta}$ is the identity tensor.

The mixture is assumed to be ideal and calorically perfect, with:

$$E = \rho \left(e + \frac{1}{2} \mathbf{u} \cdot \mathbf{u} \right), \quad (4)$$

$$p = (\gamma - 1) \rho e, \quad e = c_v T, \quad (5)$$

where e and T are respectively specific internal energy and temperature of the mixture. γ and c_v are the ratio of specific heats and specific heat at constant volume of the mixture.

The multi-component diffusive mass flux of species i is given by Hirschfelder *et al.* [20]:

$$\mathbf{J}_i = \rho \frac{M_i}{M^2} \sum_{j=1}^N M_j \tilde{D}_{ij} \nabla X_j, \quad (6)$$

where M_i and X_i are respectively the molecular weight and mole fraction of species i . M is the molecular weight of the mixture and \tilde{D}_{ij} is the mn th element of the matrix of ordinary multi-component diffusion coefficients $\tilde{\mathbf{D}}$. The mole fraction of species i is given by:

$$X_i = \frac{M}{M_i} Y_i. \quad (7)$$

Baro-diffusion is neglected in this study since the shock Mach number is relatively small [21] and after the passage of the shock the flow is close to incompressible (see below). The multi-component diffusive mass flux is reduced to the Fick's law for binary mixture:

$$\mathbf{J}_i = -\rho D_i \nabla Y_i, \quad i = 1, 2, \quad (8)$$

where $D_1 = D_2$ is the binary diffusion coefficient. Note that the Fick's law is sufficient in this work since only binary mixture is studied.

The viscous stress tensor $\boldsymbol{\tau}$ for a Newtonian mixture is:

$$\boldsymbol{\tau} = 2\mu \mathbf{S} + \left(\mu_v - \frac{2}{3} \mu \right) \boldsymbol{\delta} (\nabla \cdot \mathbf{u}), \quad (9)$$

where μ and μ_v are the shear viscosity and bulk viscosity respectively of the mixture. \mathbf{S} is the strain-rate tensor given by:

$$\mathbf{S} = \frac{1}{2} \left[\nabla \mathbf{u} + (\nabla \mathbf{u})^T \right]. \quad (10)$$

The conductive flux and the inter-species diffusional enthalpy flux [22] are given by:

$$\mathbf{q}_c = -\kappa \nabla T, \quad (11)$$

$$\mathbf{q}_d = \sum_{i=1}^N h_i \mathbf{J}_i, \quad (12)$$

where κ is the thermal conductivity of the mixture. h_i is the specific enthalpy of species i :

$$h_i = c_{p,i}T, \quad (13)$$

where $c_{p,i}$ is the specific heat at constant volume of species i .

The equations and mixing rules for the fluid properties γ , c_v , $c_{p,i}$, μ , μ_v , κ , and D_i are given in appendices A and B.

III. NUMERICAL METHODS

Simulations were performed using the in-house Hydrodynamics Adaptive Mesh Refinement Simulator (HAMeRS). The parallelization of the code and all the construction, management, and storage of cells are facilitated by the Structured Adaptive Mesh Refinement Application Infrastructure (SAMRAI) library [23–27] from Lawrence Livermore National Laboratory (LLNL). Explicit form of sixth order localized dissipation weighted compact nonlinear scheme (WCNS) [28], which is designed to add sufficient dissipation around shocks and regions with large gradients for numerical stability and minimum dissipation in smooth regions to capture vortical features, is used for the hyperbolic part of the governing equations. Explicit sixth-order finite differences are used to compute the derivatives of diffusive and viscous fluxes in non-conservative form. A third order total variation diminishing Runge-Kutta (RK-TVD) scheme [29] is adopted for time integration. Various sensors are employed to identify regions of interest for adaptive refinement. These include gradient sensor on pressure field and wavelet sensor [30] on density field to detect shock waves and mixing regions, respectively. An additional sensor based on mass fractions is also used to assist the detection of mixing regions.

IV. NUMERICAL SETUP

In our 2D numerical set-up, the height of the domain in the transverse direction is chosen to be 2.5 cm. To facilitate the comparison between 2D and 3D results in later sections, the 3D numerical set-up is chosen to be the extension of the 2D set-up with a transverse sectional area of 2.5 cm \times 2.5 cm. In both 2D and 3D simulations, a shock wave with Mach number $Ma = 1.45$ is launched initially in a sulphur hexafluoride (SF_6) region and interacts with a diffuse material interface between ideal gases SF_6 and air. The computational domain and initial conditions for the 3D simulations are shown in figure 1(b). Boundaries are periodic in the transverse directions and reflective boundary conditions are applied at the end wall. The length of the numerical shock tube is chosen to be large enough (50 cm) such that no features leave the domain at the open-sided boundary during the simulations. The 2D configuration (figure 1(a)) is basically a cross-sectional view of the 3D set-up.

The pre-shocked conditions correspond to $T = 298$ K and $p = 101325$ Pa. The fluids are initially at rest in the simulation reference frame. Table I shows the initial conditions in different portions of the domain. The initial Atwood number, $At = (\rho_{\text{SF}_6} - \rho_{\text{air}})/(\rho_{\text{SF}_6} + \rho_{\text{air}})$, across the interface is 0.68. The density, pressure, temperature, and Mach number relations across the initial shock in SF_6 in the shock reference frame are given by the Rankine-Hugoniot jump conditions:

$$\frac{\rho'}{\rho} = \frac{\left(\frac{\gamma_{\text{SF}_6}+1}{2}\right) Ma^2}{1 + \left(\frac{\gamma_{\text{SF}_6}-1}{2}\right) Ma^2}, \quad (14)$$

$$\frac{p'}{p} = \frac{2\gamma_{\text{SF}_6} Ma^2 - 1}{\frac{\gamma_{\text{SF}_6}+1}{\gamma_{\text{SF}_6}-1}}, \quad (15)$$

$$\frac{T'}{T} = \left(\frac{\gamma_{\text{SF}_6} Ma^2 - \left(\frac{\gamma_{\text{SF}_6}-1}{2}\right)}{\frac{\gamma_{\text{SF}_6}+1}{2}}\right) \left(\frac{1 + \left(\frac{\gamma_{\text{SF}_6}-1}{2}\right) Ma^2}{\left(\frac{\gamma_{\text{SF}_6}+1}{2}\right) Ma^2}\right), \quad (16)$$

$$Ma'^2 = \left(\frac{1 + \left(\frac{\gamma_{\text{SF}_6}-1}{2}\right) Ma^2}{\gamma_{\text{SF}_6} Ma^2 - \left(\frac{\gamma_{\text{SF}_6}-1}{2}\right)}\right), \quad (17)$$

where quantities without primes are pre-shock quantities and those with primes are post-shock quantities.

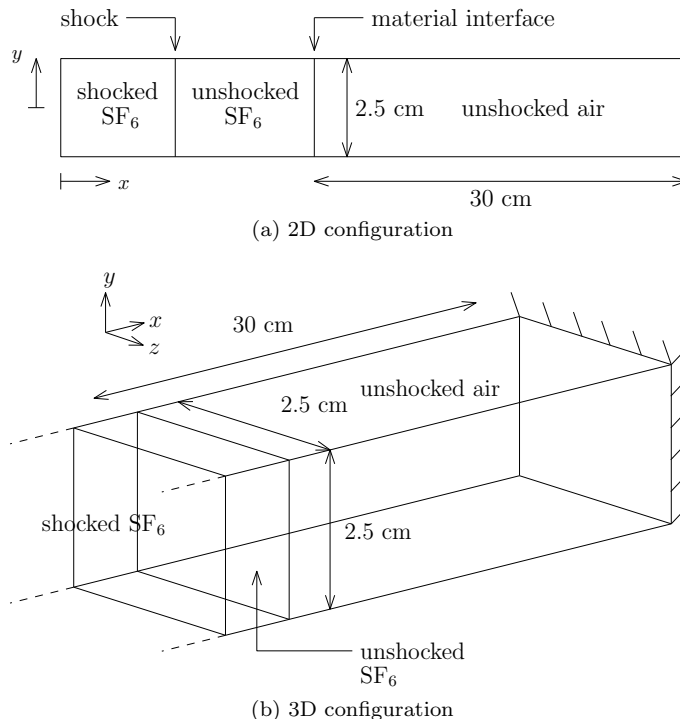


FIG. 1. Schematic diagrams of initial flow fields and computational domains for the 2D and 3D simulations.

TABLE I. Initial conditions of the post-shock state and the pre-shock states of the light- and heavy-fluid sides.

Quantity	Post-shock SF ₆	Pre-shock SF ₆	Air
ρ (kg m ⁻³)	11.97082	5.972866	1.145601
p (Pa)	218005.4	101325.0	101325.0
T (K)	319.9084	298.0	298.0
u (m s ⁻¹)	98.93441	0.0	0.0

Figure 2 shows the space-time ($x-t$) diagram for different features in a one-dimensional (1D) flow representation. $t = 0$ is set as the instance of the first arrival of the shock at the interface. The initial position of the incident shock is chosen such that the first shock-interface interaction occurs at 0.05 ms after the start of simulation. Since the shock traverses the interface from the heavy fluid side, a shock is transmitted to the light fluid side and a rarefaction wave is reflected back to the heavy fluid side. The shock wave also accelerates the interface towards the end wall. After hitting the end wall, the shock is reflected back and interacts with the interface again at $t \approx 1.15$ ms. Since the reflected shock passes from the light fluid side during the re-shock of interface, a transmitted shock and a reflected shock are generated. The reflected shock will eventually lead to a second re-shock. The simulations are stopped at $t = 1.75$ ms, which is the time just before second re-shock, as the grid resolution requirements become too large to accurately capture this flow stage.

In order to trigger the flow instability, perturbations are seeded on the material interfaces. Multi-mode perturbations for 2D and 3D simulations are given by the following two equations:

$$S(y) = A \sum_m \cos\left(\frac{2\pi m}{L_y} y + \phi_m\right), \quad (18)$$

$$S(y, z) = A \sum_m \cos\left(\frac{2\pi m}{L_{yz}} y + \phi_m\right) \cos\left(\frac{2\pi m}{L_{yz}} z + \psi_m\right), \quad (19)$$

where $L_y = L_{yz} = 2.5$ cm. In both 2D and 3D simulations, there are 11 perturbation modes with wavenumber m between 20 and 30 in each transverse direction. Constant amplitude $A = \sqrt{2} \times 0.01$ mm is used for each mode and random phase shifts ϕ_m and ψ_m between 0 and 2π are added to each mode to prevent adding up of harmonics.

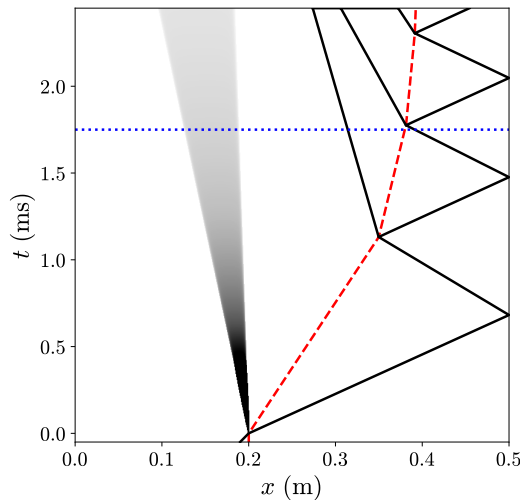


FIG. 2. x - t diagram showing the propagation of material interface, shock waves, and rarefaction. Red dashed line: material interface; black lines: shock waves; gray region: rarefaction. The blue dotted line indicates the end time of all simulations.

A finite thickness is prescribed for the initial interface between SF_6 and air. The partial density of each gas, ρY_i , is smoothed across the material interface initially with the following formulation:

$$f_{sm} = \frac{1}{2} \left(1 + \operatorname{erf} \left(\frac{x - L_i - S}{\epsilon_i} \right) \right), \quad (20)$$

$$(\rho Y_i)_{sm} = (\rho Y_i)_L (1 - f_{sm}) + (\rho Y_i)_R f_{sm}, \quad (21)$$

where L_i is the initial location of the material interface. ϵ_i is the characteristic thickness of the initial material interface and is set to 1 mm.

To reduce the statistical variability associated with the very few modes present at the 1D interface, all statistical results for the 2D simulations are obtained by ensemble averaging over 24 realizations with different random phase shifts ϕ_m in the initial perturbations.

V. CHARACTERISTIC SCALES OF TWO-DIMENSIONAL AND THREE-DIMENSIONAL PROBLEMS

In this section, the characteristic length scales, time scales, and growth rates of the 2D and 3D problems are determined from the initial conditions and the linear theory.

The growth rate $\dot{\eta}_{imp}^{2D}$ for a 2D small single-mode perturbation with initial amplitude η_0^{2D} from an impulsive acceleration on a discontinuous interface obtained from linear theory by Richtmyer [1] is given by:

$$\dot{\eta}_{imp}^{2D} = \frac{2\pi}{\lambda^{2D}} U_i A t \eta_0^{2D}, \quad (22)$$

where λ^{2D} is the wavelength of the perturbation and U_i is the change in interface velocity induced by the incident shock wave. It can be extended to the growth rate of a 3D single-mode interface as:

$$\dot{\eta}_{imp}^{3D} = \sqrt{2} \frac{2\pi}{\lambda^{3D}} U_i A t \eta_0^{3D}, \quad (23)$$

where $\lambda^{3D} = \lambda_y^{3D} = \lambda_z^{3D}$ is the wavelength of the perturbation in either y or z directions.

Although material interfaces are smoothed initially in the numerical setup, the growth rates from linear theory still become relevant after the initial diffusive growth. In this work, the amplitudes η_0^{2D} and η_0^{3D} are estimated as the standard deviations of the initial perturbations.

The wavelengths λ^{2D} and λ^{3D} can be estimated from the integral length scales. Since the initial perturbations are periodic with only few modes, the integral length scales are computed from the energy spectra of the perturbations, instead of the autocorrelations. This is necessary, as the autocorrelation of a periodic signal is itself periodic and does

not approach zero when based on only few modes, no matter how large the computational domain is. The integral length scales for the 2D and 3D cases, l^{2D} and l^{3D} , are computed as:

$$l^{2D}/l^{3D} = \frac{2\pi}{\int_0^\infty E(k) dk} \int_0^\infty \frac{E(k)}{k} dk, \quad (24)$$

where $E(k)$ is the energy spectrum of the perturbation that depends on angular wavenumber k . Note that $E(k)$ is the radial energy spectrum in the yz plane and k is the radial angular wavenumber for the 3D case. The wavelengths λ^{2D} and λ^{3D} are then estimated as:

$$\lambda^{2D} = l^{2D}, \quad \lambda^{3D} = \sqrt{2}l^{3D}. \quad (25)$$

The characteristic time scales can be obtained from the impulsive growth rates as:

$$\tau^{2D} = \frac{\lambda^{2D}}{\dot{\eta}_{imp}^{2D}}, \quad \tau^{3D} = \frac{\lambda^{3D}}{\dot{\eta}_{imp}^{3D}}. \quad (26)$$

Table II shows the standard deviations, wavelengths, growth rates from impulsive theory, and characteristic time scales from the initial conditions of the 2D and 3D cases. It can be seen from the table that the growth rates and characteristic time scales for both 2D and 3D cases are virtually identical with the initial conditions chosen.

TABLE II. Initial characteristic scales for the 2D and 3D cases.

Case	η_0 (mm)	λ (mm)	$\dot{\eta}_{imp}$ (m s ⁻¹)	τ (ms)
2D	0.0331	1.02	18.4	0.0552
3D	0.0234	1.02	18.4	0.0551

VI. GRID SENSITIVITY ANALYSIS

To understand the sensitivities of numerical results to the grid spacing, a grid sensitivity study is conducted for both 2D and 3D problems. Tables III and IV show the grids used in the grid sensitivity analysis. In all grid settings, there are three levels of meshes in total, with two levels of mesh refinement. The refinement ratios in each direction are respectively 1:2 and 1:4 from base level to second level and from second level to the finest level. For the 2D problem, the base grids have number of grid points in the transverse direction varying from 128 points (grid D) to 1024 points (grid G). The highest resolution grid has grid spacing of 3.05 μm at the finest level. 24 realizations are conducted on each grid to reduce the statistical variability of the data. As for the 3D problem, the base grids have number of grid points in the transverse directions varying from 32 points (grid B) to 128 points (grid D). The highest resolution grid has grid spacing of 24.4 μm at the finest level. Figure 3 shows the visualization of the mixing layer with the shock wave and the adaptive mesh refinement (AMR) grid for the 3D problem just before re-shock during the simulation with grid D.

TABLE III. Different grids used for the 2D problem. Three levels of grids, with 1:8 overall refinement ratio in each direction, are used in all cases.

Grid	Base grid resolution	Refinement ratios	Finest grid spacing (μm)
D	2560 \times 128	1:2, 1:4	24.4
E	5120 \times 256	1:2, 1:4	12.2
F	10240 \times 512	1:2, 1:4	6.10
G	20480 \times 1024	1:2, 1:4	3.05

The grid sensitivities of different statistical quantities are examined through comparison of their temporal evolution corresponding to different grids. The quantities analyzed include the mixing width, W , mixedness, Θ , integrated turbulent kinetic energy, TKE, integrated scalar dissipation rate, χ , and integrated enstrophy, Ω . The mixing width and mixedness are defined as:

$$W = \int 4\bar{X}_{\text{SF}_6} (1 - \bar{X}_{\text{SF}_6}) dx, \quad (27)$$

$$\Theta = \frac{\int \bar{X}_{\text{SF}_6} (1 - \bar{X}_{\text{SF}_6}) dx}{\int \bar{X}_{\text{SF}_6} (1 - \bar{X}_{\text{SF}_6}) dx}, \quad (28)$$

TABLE IV. Different grids used for the 3D problem. Three levels of grids with 1:8 overall refinement ratio in each direction are used in all cases.

Grid	Base grid resolution	Refinement ratios	Finest grid spacing (μm)
B	$640 \times 32 \times 32$	1:2, 1:4	97.7
C	$1280 \times 64 \times 64$	1:2, 1:4	48.8
D	$2560 \times 128 \times 128$	1:2, 1:4	24.4

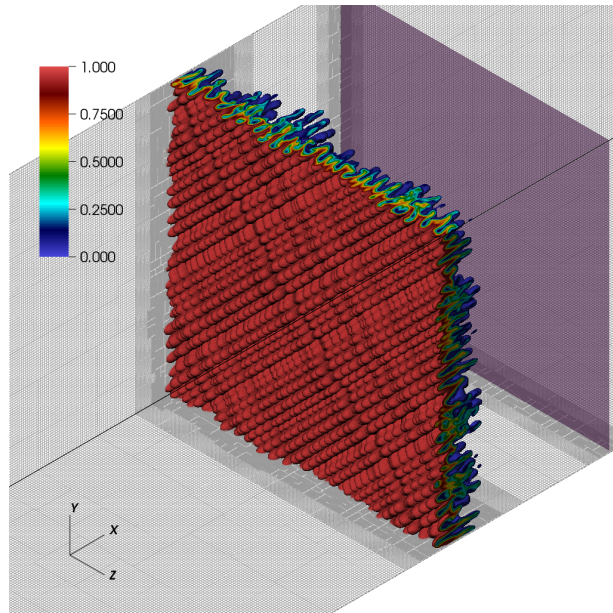


FIG. 3. Isovolume of the SF_6 mole fraction, X_{SF_6} , at $t = 1.10$ ms for the 3D problem with grid D. The colorbar indicates the value of X_{SF_6} . The transparent magenta plane represents the location of shock. The AMR grid hierarchy is shown on the side walls of the domain.

where $\bar{\cdot}$ is the mean of the respective quantity in the homogeneous directions (y direction for 2D and yz plane for 3D). The mean is also computed using an additional averaging over the 24 realizations (ensemble averaging) for the 2D case.

The mathematical formulations for TKE, scalar dissipation rate, and enstrophy are given by:

$$\text{TKE} = \frac{1}{2} \rho u_i'' u_i'', \quad (29)$$

$$\chi = D_{\text{SF}_6} \nabla Y_{\text{SF}_6} \cdot \nabla Y_{\text{SF}_6}, \quad (30)$$

$$\Omega = \rho \boldsymbol{\omega} \cdot \boldsymbol{\omega}, \quad (31)$$

where $u_i'' = u_i - \tilde{u}_i$ and $\boldsymbol{\omega} = \nabla \times \mathbf{u}$ is the vorticity. The Favre (density-weighted) mean of the velocity is defined by $\tilde{u}_i = \overline{\rho u_i} / \bar{\rho}$. The integrated quantities are calculated over the full domain.

Figures 4 and 5 show the time evolution of various statistical quantities computed on different grids for the 2D and 3D cases, respectively. The mixing width defines the large-scale characteristic length of the mixing layer. The growth of this quantity is largely dominated by the entrainment of the fluids through convective motions. The mixedness measures the amount of fluids that is molecularly mixed within the mixing layer. It can be regarded as the ratio of the amount of fluids molecularly mixed to the amount of fluids entrained by convection. By comparing the results obtained on grids F and G from figure 4, it can be seen that both mixing width and mixedness for the 2D case are fully grid converged. Similarly, for the 3D case, it can be seen from figure 5 that the grid also has very little effect on the mixing width and mixedness at the highest grid resolution level (grid D).

In the flow problem being studied, kinetic energy is deposited at the material interface when the shock passes through the interface and TKE is generated subsequently. TKE is largely dominated by the low wavenumber eddies or large scale features. After the passage of the shock, TKE decays as it is converted to internal energy through viscous dissipation. Grid convergence of the domain-integrated TKE is obtained at the highest resolutions considered for both 2D and 3D problems, as seen in figures 4 and 5.

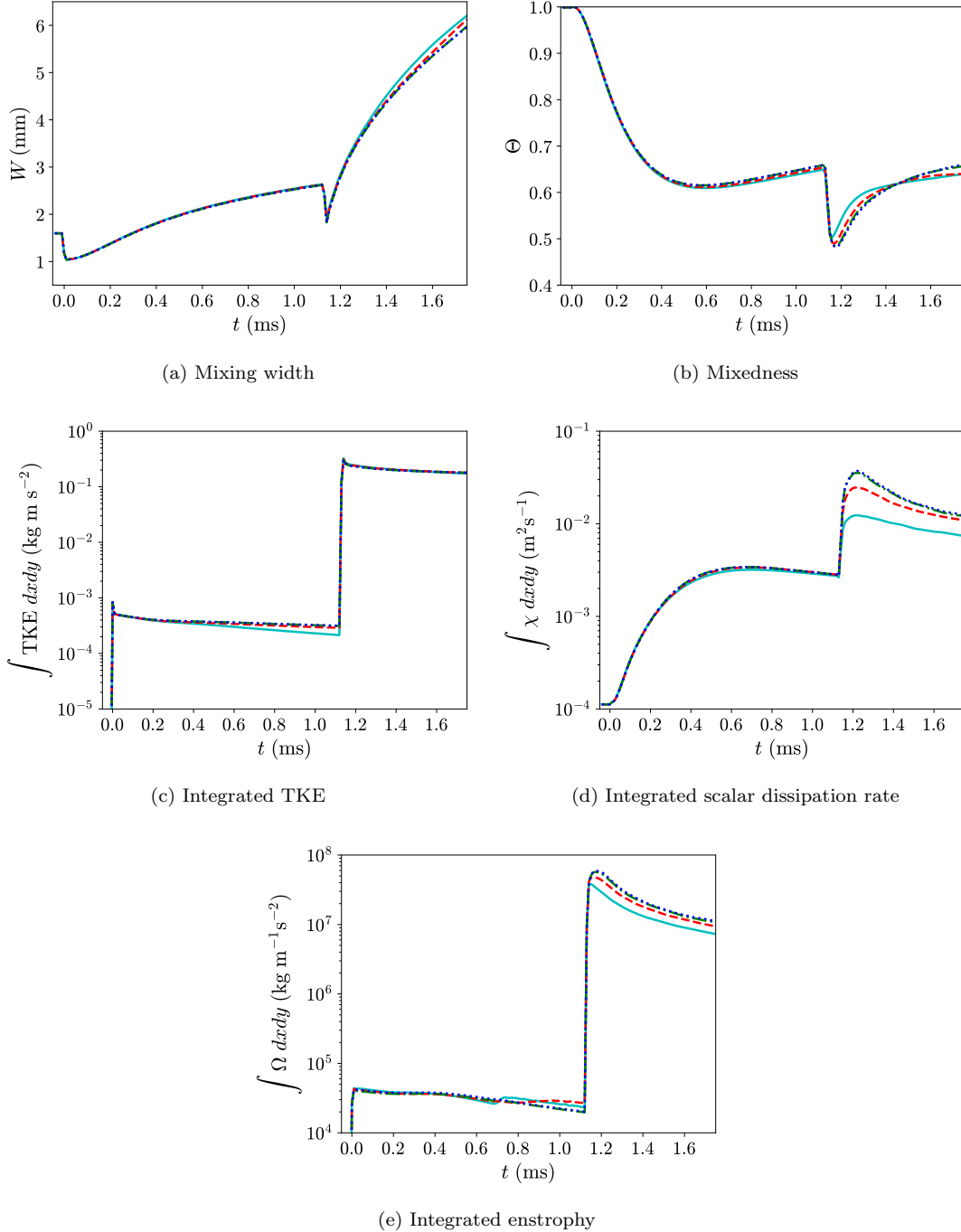


FIG. 4. Grid sensitivities of different statistical quantities over time for the 2D problem. Cyan solid line: grid D; red dashed line: grid E; green dash-dotted line: grid F; blue dotted line: grid G.

While mixing width and TKE are dominated by large scale features, scalar dissipation rate and enstrophy are mainly associated with high wavenumber features closer to Batchelor and Kolmogorov scales. Therefore, the grid convergence requirements for these two quantities are expected to be stricter than mixing width and TKE. From figure 4, we can see that grid convergence for both domain-integrated scalar dissipation rate and enstrophy is still achieved for the 2D problem, but only at the finest grid. For the 3D problem, grid convergence of both integrated quantities is only obtained for a short duration after first shock (until $t \approx 0.25$ ms) with the finest grid.

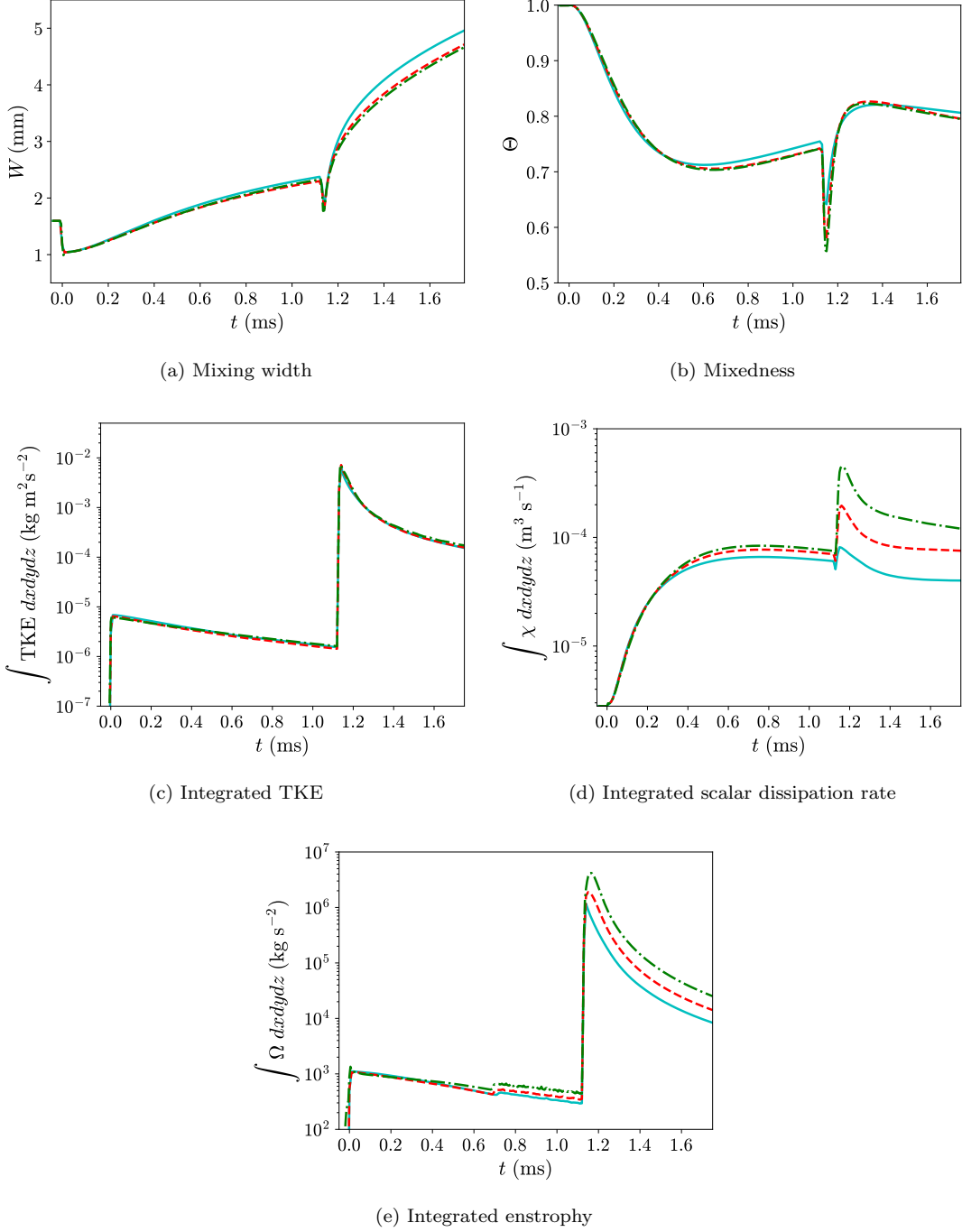


FIG. 5. Grid sensitivities of different statistical quantities over time for the 3D problem. Cyan solid line: grid B; red dashed line: grid C; green dash-dotted line: grid D.

VII. SET-UP FOR THREE-DIMENSIONAL SIMULATIONS WITH REDUCED REYNOLDS NUMBERS

In order to study the effect of the Reynolds number on the development of 3D RMI, the 3D problem presented in the previous sections is repeated with the same initial conditions, but with increased transport coefficients for each species (D_i , μ_i , $\mu_{v,i}$, and κ_i). The transport coefficients are increased in the simulations by artificially multiplying the values computed using physical models given in appendix A with constant factors. Two cases, with transport

coefficients increased by factors of 2 and 4, are simulated.

Figure 6 shows the time evolution of the means of the Reynolds numbers based on the mixing width, W , and mean integral length scale of SF_6 mole fraction, $\langle l_{X_{\text{SF}_6}} \rangle$, ($\langle Re_W \rangle$ and $\langle Re_l \rangle$), Schmidt number ($\langle Sc \rangle$), and Prandtl number ($\langle Pr \rangle$). The mean denoted by $\langle \cdot \rangle$ corresponds to an additional averaging over the central part of the mixing layer of the quantities computed over the lines or planes. Re_W , Re_l , Sc , and Pr are defined as:

$$Re_W = \frac{\bar{\rho} u_{\text{rms}} W}{\bar{\mu}}, \quad (32)$$

$$Re_l = \frac{\bar{\rho} u_{\text{rms}} \langle l_{X_{\text{SF}_6}} \rangle}{\bar{\mu}}, \quad (33)$$

$$Sc = \frac{\bar{\mu}}{\bar{\rho} \bar{D}_{\text{SF}_6}}, \quad (34)$$

$$Pr = \frac{\bar{c}_p \bar{\mu}}{\bar{\kappa}}, \quad (35)$$

where $u_{\text{rms}} = \sqrt{u_i'' u_i'' / 3}$. The central part of the mixing layer is defined as the regions where cross-sectional planes satisfy:

$$4\bar{X}_{\text{SF}_6} (1 - \bar{X}_{\text{SF}_6}) \geq 0.9. \quad (36)$$

The nondimensional time, t^* , is defined by:

$$t^* = \frac{t}{\tau_c}, \quad (37)$$

where $\tau_c = \tau^{3D}$. Figure 6 shows that increasing the transport coefficients mostly affects the Reynolds numbers, while other non-dimensional quantities such as Schmidt and Prandtl numbers within the central part of mixing layer remain almost unchanged over time. The Reynolds number values are close when calculated based on the mixing width or integral length scale since these length scales have similar orders of magnitude. The simulations with reduced Reynolds numbers are further discussed in the next section.

VIII. COMPARISON AND ANALYSIS OF TWO-DIMENSIONAL AND THREE-DIMENSIONAL CASES

This section contains the main results of the paper. First, the levels of compressibility and non-Boussinesq effects are assessed using the turbulent Mach number and an effective Atwood number. Then, some features of the mixing are discussed using the mean and variance profiles of the mole fraction as well as its probability density function. This is then followed by a discussion of the turbulent kinetic energy and the anisotropy of Reynolds normal stresses. Finally, the time evolution of the spectra of the mole fraction and energy defined based on the momentum with density-weighted fluctuation of the velocity after re-shock is examined.

A. Flow compressibility and effective Atwood number

Several aspects of compressibility of a flow can be measured from the turbulent Mach number, Ma_t , which is defined as:

$$Ma_t = \frac{\sqrt{u_i'' u_i''}}{\bar{c}}, \quad (38)$$

where $c = \sqrt{\gamma p / \rho}$ is the speed of sound.

Figure 7 shows the time evolution of turbulent Mach number within the central part of the mixing layer for the 2D and 3D cases with different transport coefficients. The turbulent Mach number is very close to zero for all cases before re-shock. After re-shock, the turbulent Mach number for all 3D cases decays quickly to zero asymptotically after a jump. The turbulent Mach number for the 2D case is larger than that for the 3D cases because velocity fluctuations remain larger in the 2D case after re-shock. This is further discussed in section VIII F. Overall though, all simulations are only weakly compressible as $\langle Ma_t \rangle$ for each case is always smaller than 0.3.

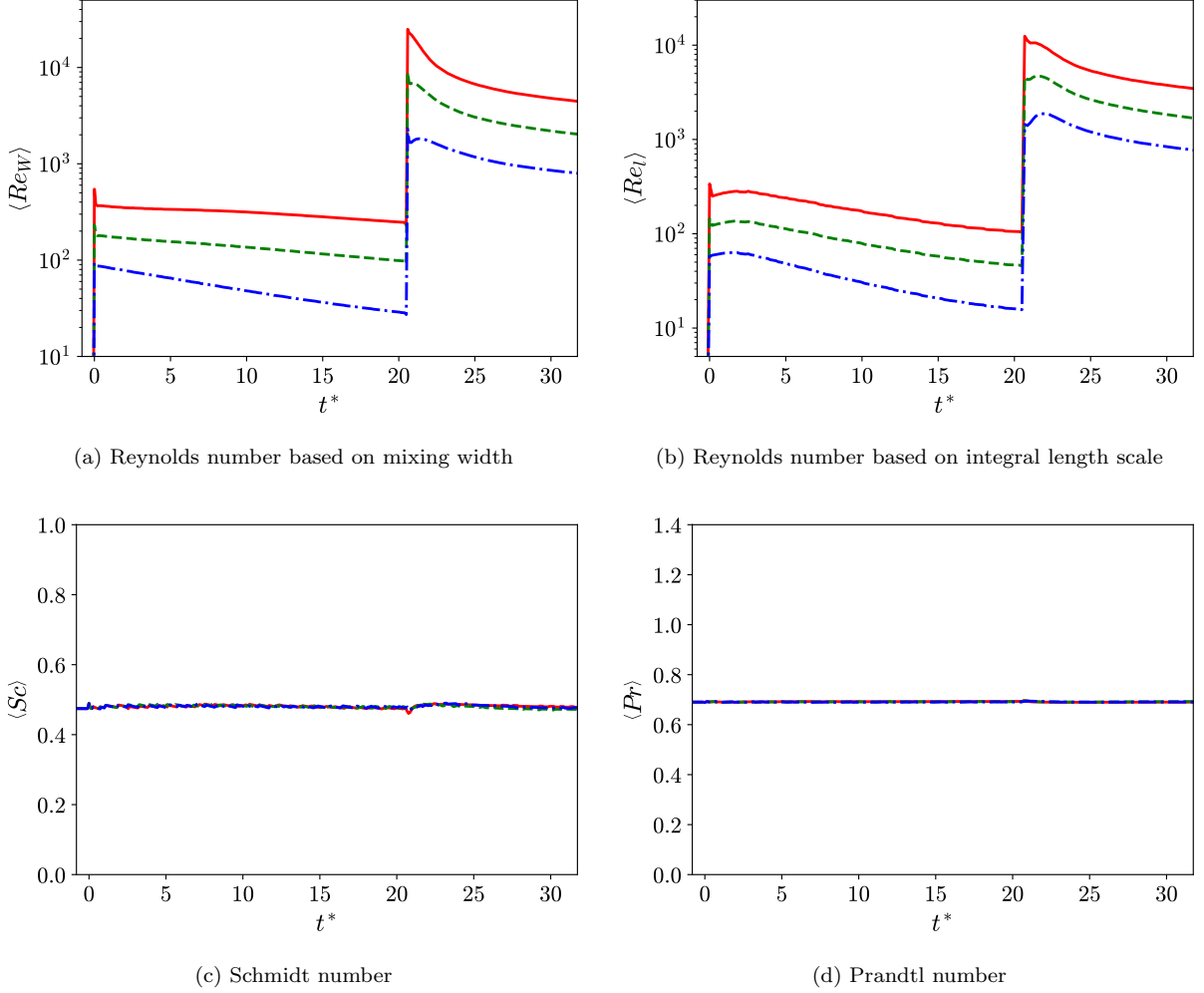


FIG. 6. Comparison of the time evolution of different dimensionless numbers between the 3D cases with different transport coefficients. Red solid line: physical transport coefficients; green dashed line: $2\times$ physical transport coefficients; blue dash-dotted line: $4\times$ physical transport coefficients.

Another measure of the compressibility effects is the magnitudes of thermodynamic fluctuations. From the ideal equation of state, the mixture density, ρ , depends on pressure, p , mixture molecular weight, M , and temperature, T , through $\rho = pM/(R_u T)$. Figure 8 shows the normalized covariances of ρ with p , M , and $1/T$ across the normalized position x^* just after first shock and re-shock from the 2D and 3D simulations with physical transport coefficients. The normalized position is defined as:

$$x^*(x, t) = \frac{x - x_i(t)}{W(t)}, \quad (39)$$

where x_i is the location of the interface from the $x-t$ diagram (figure 2). It is shown in figure 8 that, for both cases, the covariance of the mixture density and mixture molecular weight is the largest among the three covariances at the two times just after impulsive accelerations considered. Compared to this covariance, the covariance of the mixture density and reciprocal of temperature is much smaller and that of the mixture density and pressure is virtually zero, which means the mixing layer is very weakly compressible.

As a consequence of the near incompressible flow behavior, from the ideal equation of state density mainly depends on the composition of the flow through the mixture molecular weight, M , as the quantity $\rho R_u/M = p/T$, is very uniform across the mixing region, where R_u is the universal gas constant. This is consistent with the derivation of the variable-density Navier-Stokes equations as the infinite speed of sound limit of the fully compressible Navier-Stokes equations with multi-species transport [21]. Similar to the variable-density incompressible limit, if the ratio p/T is constant, one can also easily derive a linear relationship between mole fraction and density as:

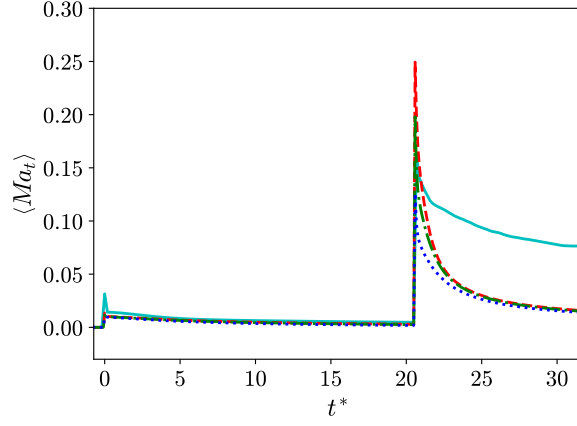


FIG. 7. Comparison of the time evolution of means of turbulent Mach number, $\langle Ma_t \rangle$, in the central part of mixing layer between the 2D and 3D problems. Cyan solid line: 2D with physical transport coefficients; red dashed line: 3D with physical transport coefficients; green dash-dotted line: 3D with $2\times$ physical transport coefficients; blue dotted line: 3D with $4\times$ physical transport coefficients.

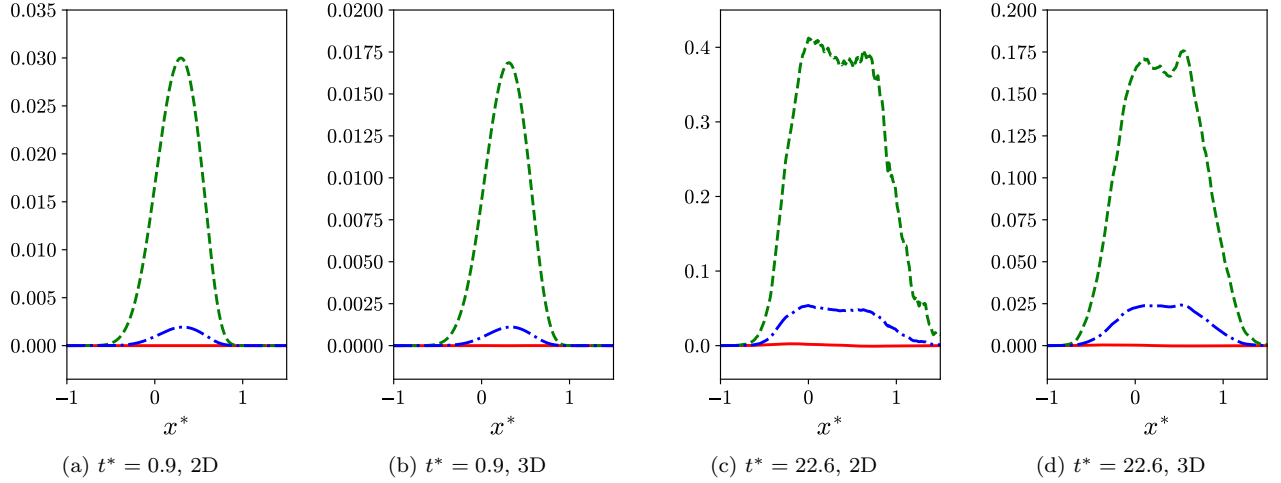


FIG. 8. Profiles of normalized covariances of mixture density with other quantities just after first shock ($t^* = 0.9$) and just after re-shock ($t^* = 22.6$) for the 2D and 3D problems with physical transport coefficients. Red solid line: $\overline{\rho'p'}/(\overline{\rho p})$; green dashed line: $\overline{\rho'M'}/(\overline{\rho M})$; blue dash-dotted line: $\overline{\rho'(1/T)'}/(\overline{\rho(1/T)})$.

$$X_{\text{SF}_6} = \frac{\rho - \rho_{\text{air}}}{\rho_{\text{SF}_6} - \rho_{\text{air}}}, \quad (40)$$

or

$$\rho = (\rho_{\text{SF}_6} - \rho_{\text{air}}) X_{\text{SF}_6} + \rho_{\text{air}}, \quad (41)$$

where ρ_{air} and ρ_{SF_6} are time-dependent densities of air and SF_6 , respectively, on either side of the material interface from the solutions of the 1D flow representation. ρ_{air} and ρ_{SF_6} only change at first shock and re-shock. Figure 9 compares the ratios between the density mean profiles reconstructed from the mole fraction mean profiles using equation (41) and the true density mean profiles for the 2D and 3D cases with physical transport coefficients at different times. Both 2D and 3D flows are near incompressible as the density ratios have less than 5% deviation from one at all times. The quasi-linear relationship between mole fraction and density suggests that mole fraction field can be viewed as normalized density field within the mixing region.

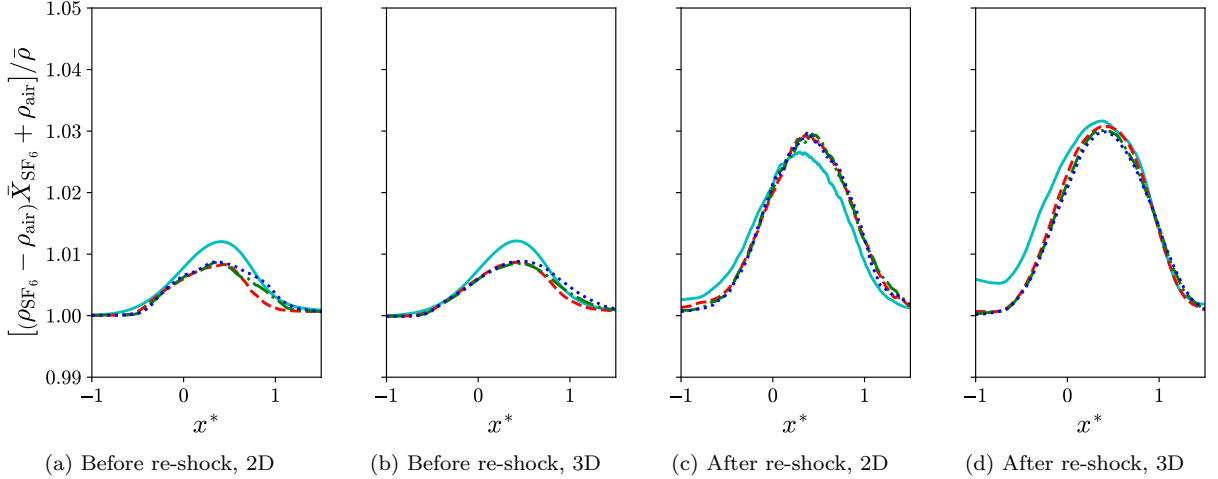


FIG. 9. Profiles of the ratio between the reconstructed density using the incompressible assumption and true density at different times for the 2D and 3D problems with physical transport coefficients. Before re-shock: $t^* = 0.9$ (cyan solid line); $t^* = 7.5$ (red dashed line); $t^* = 14.1$ (green dash-dotted line); $t^* = 20.7$ (blue dotted line). After re-shock: $t^* = 22.6$ (cyan solid line); $t^* = 26.3$ (red dashed line); $t^* = 30.1$ (green dash-dotted line); $t^* = 32.9$ (blue dotted line).

To quantify the non-Boussinesq effects inside the mixing layer, we can study the effective Atwood number, At_e , within the central part of the mixing layer, which is defined by Cook *et al.* [31] as:

$$At_e = \left\langle \frac{\sqrt{\rho'^2}}{\bar{\rho}} \right\rangle. \quad (42)$$

The Boussinesq approximation is invalid if $At_e \geq 0.05$. Since the flows are nearly incompressible, the effective Atwood number is in fact also related to the mole fraction through equation (41):

$$At_e \approx \left\langle \frac{\sqrt{X'_{SF_6}{}^2}}{\bar{X}_{SF_6} + \rho_{air} / (\rho_{SF_6} - \rho_{air})} \right\rangle. \quad (43)$$

Figure 10 shows the effective Atwood number computed with equation (42) against time. Before first shock, At_e is small and very different from the Atwood number of a discontinuous interface (0.68), since the material interface is smoothed initially. However, after first shock, At_e increases rapidly as the interface becomes sharper, followed by gradual decrease due to molecular diffusion. After re-shock, there is a jump in At_e due to further interface intensification. At_e seems to plateau at late times in all cases. The flows in all cases are very non-Boussinesq after the first shock. In general, the mixing layer is more non-Boussinesq in the 2D configuration than in the 3D configuration, as At_e is always larger for the 2D case.

B. Visualization of mole fraction fields

Figures 11 and 12 show the SF_6 mole fraction fields for the 2D and 3D problems at different normalized times t^* . The development of the bubble and spike structures is very similar at early times after first shock for both cases. As time evolves, the differences in the development of the instability become more distinguishable. In the 2D case, many mushroom structures, which are caused by the roll-up of the interface due to baroclinic torque can be observed. In the 3D case, the roll-up of the interface is less prominent. Instead, the bubble and spike grow into long structures at the moment just before re-shock. Right after re-shock, at $t^* \approx 21.5$, there is an immediate enhancement in mixing for both cases. However, the distinction between the 2D and 3D cases remains clear. In the 3D case, particular structures can no longer be identified, which is indicative of the mixing transition. On the contrary, distinct mushroom dipole structures can still be observed for the 2D case, although the flow field becomes much more chaotic than the state just before re-shock.

Figures 12, 13 and 14 compare the SF_6 mole fraction fields from the 3D simulations with different transport coefficients. Before re-shock, features are smeared out for cases with increased transport coefficients, as the viscous

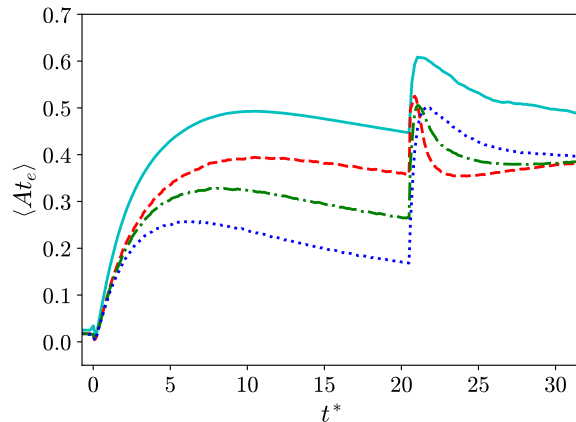


FIG. 10. Comparison of the time evolution of means of effective Atwood number, $\langle At_e \rangle$, in the central part of mixing layer between the 2D and 3D problems. Cyan solid line: 2D with physical transport coefficients; red dashed line: 3D with physical transport coefficients; green dash-dotted line: 3D with $2\times$ physical transport coefficients; blue dotted line: 3D with $4\times$ physical transport coefficients.

and diffusive effects are acting on faster time scales relative to those of the inviscid linear and nonlinear instability effects. After re-shock, the mixing transitions are delayed for the reduced Reynolds number cases. This is most clear for the case with 4 times increase in transport coefficients. Right after re-shock, at $t^* = 22.6$, features maintaining coherence can still be observed. Nevertheless, based on the visual inspection of the figures, turbulent mixing is observed at the end times for all simulations, indicating that mixing transitions occur in all cases.

C. Mole fraction profiles and mixing widths

Figure 15 shows the mean profiles of SF_6 mole fraction, \bar{X}_{SF_6} , from the 2D and 3D simulations with physical transport coefficients at different times. The mean mole fraction profiles collapse quite well at late times after both first shock and re-shock for both 2D and 3D cases. The profiles are asymmetric, as the spikes penetrate more than the bubbles. Similar findings were also observed for the density profiles in the planar Rayleigh-Taylor (RT) instability, or RTI, studied by Livescu *et al.* [32, 33]. It is also interesting to see that the normalized density profiles at late times become quite indistinguishable for both 2D and 3D cases.

The development of the mixing widths for the 2D and 3D cases is compared in figure 16(a). The mixing width is normalized by $\hat{\eta}_{imp}$ and τ_c :

$$W^* = \frac{W - W|_{t=0}}{\hat{\eta}_{imp}\tau_c}. \quad (44)$$

With physical transport coefficients, W^* initially grows at a slightly faster rate in the 2D case compared to the 3D case after first shock, but the growth rates become similar before re-shock. After re-shock, the 2D mixing width grows at a much higher rate than the 3D mixing width until the end of simulations. Comparing the 3D cases with different transport coefficients on the same figure, it can be seen that although the growths of the normalized mixing widths are very similar just after first shock, they become smaller with decreasing Reynolds number until re-shock. After re-shock, the growth rates are very similar and almost identical at the end of simulations among all 3D cases.

D. Mixedness and mole fraction variance profiles

The time evolution of mixedness is different for the 2D and 3D cases, as seen in figure 16(b). After first shock, from $t^* = 0$ to $t^* = 5$, the mixedness decreases for all cases, as the interface stretches due to rapid gradient intensification, while molecular diffusion is not fast enough to counteract this process. With physical transport coefficients, the 2D mixedness decreases at a faster rate than the 3D mixedness after first shock. At later times after first shock and before the re-shock, the mixedness of all cases increases again, as the rate of molecular mixing becomes larger than the rate of entraining pure fluids. Comparing the 3D cases before re-shock, it can be seen that mixedness increases

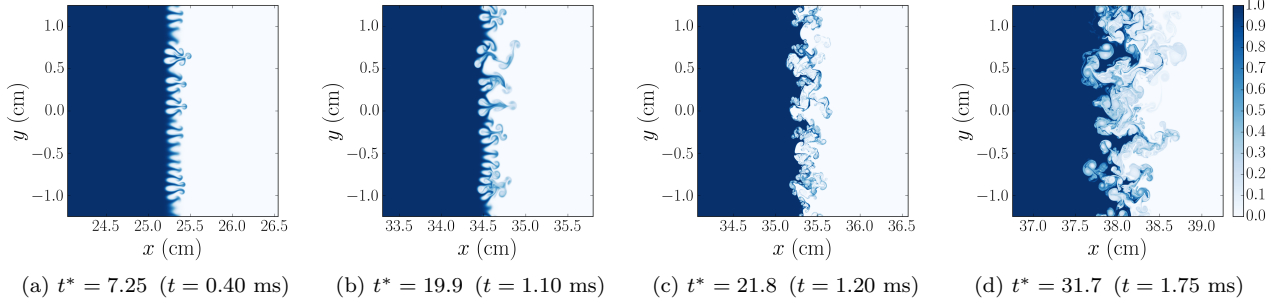


FIG. 11. SF_6 mole fraction fields, X_{SF_6} , at different times from one of the realizations for the 2D problem computed with grid G.

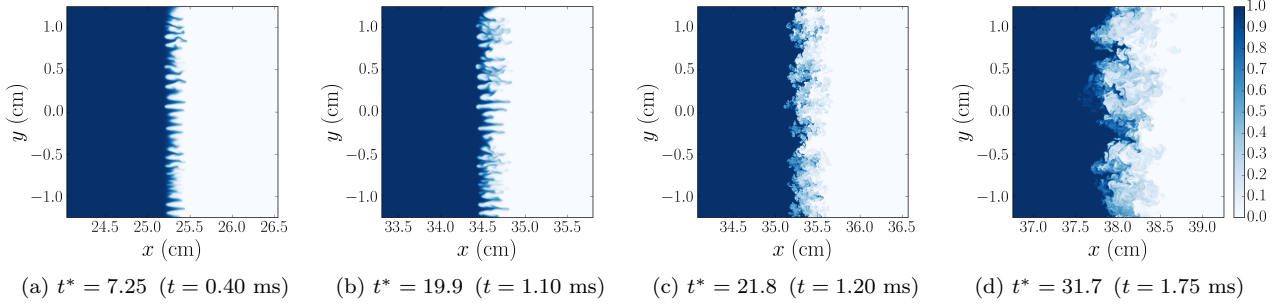


FIG. 12. SF_6 mole fraction fields, X_{SF_6} , in xy plane at $z = 0$, at different times for the 3D problem with physical transport coefficients computed with grid D.

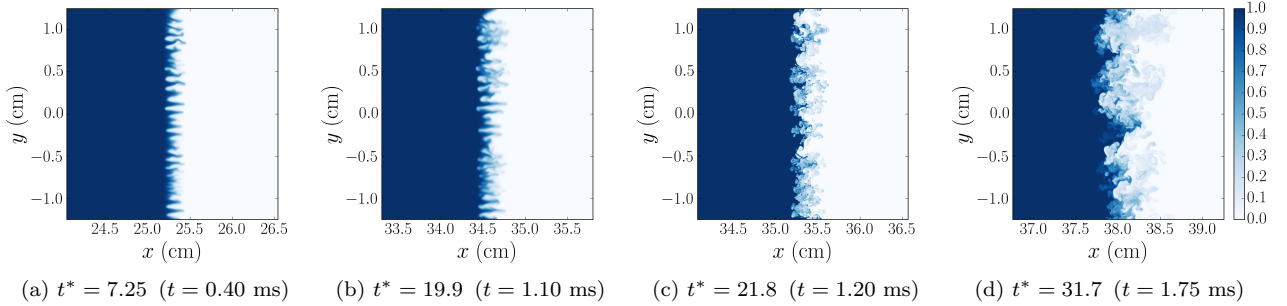


FIG. 13. SF_6 mole fraction fields, X_{SF_6} , in xy plane at $z = 0$, at different times for the 3D problem with $2\times$ physical transport coefficients computed with grid D.

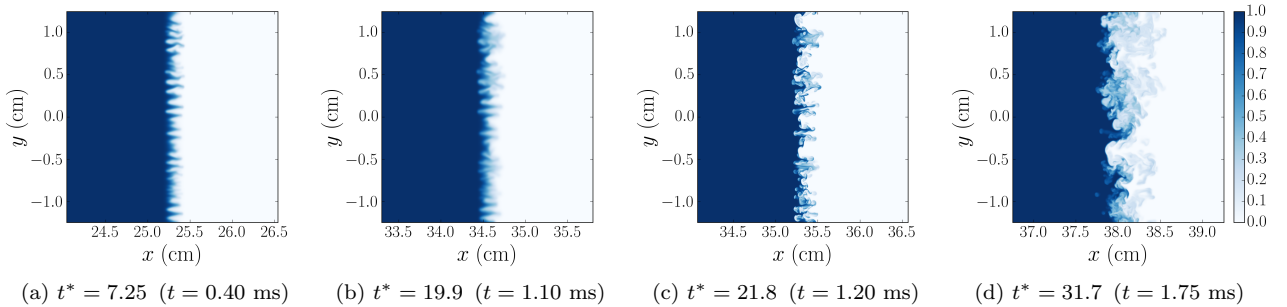


FIG. 14. SF_6 mole fraction fields, X_{SF_6} , in xy plane at $z = 0$, at different times for the 3D problem with $4\times$ physical transport coefficients computed with grid D.

with decreasing Reynolds number because of larger molecular diffusion inside the mixing region. After re-shock, there is a sudden decrease in mixedness in all cases as the interface stretches again due to gradient intensification. However,

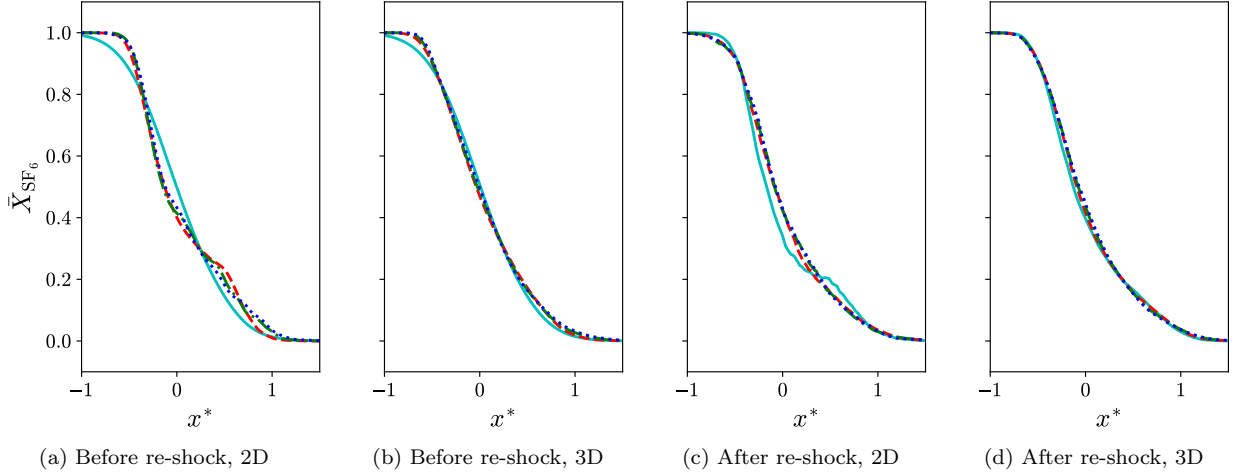


FIG. 15. Profiles of SF₆ mole fraction, \bar{X}_{SF_6} , at different times for the 2D and 3D problems with physical transport coefficients. Before re-shock: $t^* = 0.91$ (cyan solid line); $t^* = 7.25$ (red dashed line); $t^* = 13.6$ (green dash-dotted line); $t^* = 19.9$ (blue dotted line). After re-shock: $t^* = 21.8$ (cyan solid line); $t^* = 25.4$ (red dashed line); $t^* = 29.0$ (green dash-dotted line); $t^* = 31.7$ (blue dotted line).

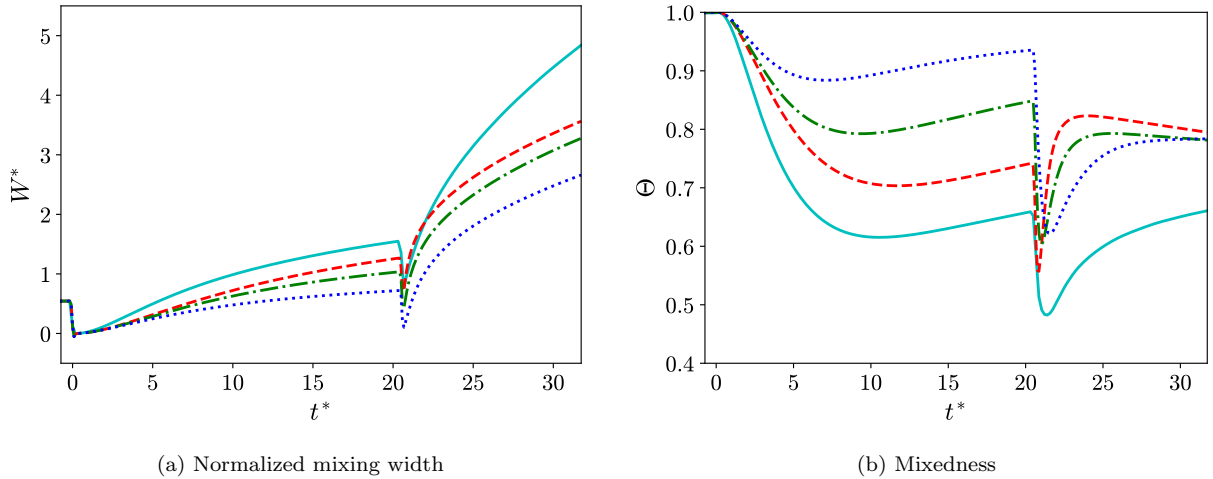


FIG. 16. Comparison of the time evolution of mixing quantities between the 2D and 3D problems. Cyan solid line: 2D with physical transport coefficients; red dashed line: 3D with physical transport coefficients; green dash-dotted line: 3D with $2\times$ physical transport coefficients; blue dotted line: 3D with $4\times$ physical transport coefficients.

the mixedness recovers soon after the sudden reduction of mixedness in all cases. Comparing the 2D and 3D cases with physical transport coefficients, mixedness of the 3D case increases at a faster rate. This is likely associated with turbulent mixing in the 3D case, while transition to turbulence is absent in the 2D case. At late times after re-shock, mixedness for all 3D cases seems to approach to the same asymptotic value of around 0.8. For the 2D case, the mixedness approaches a different value at around 0.7. Similar asymptotic values of mixedness in 3D configurations were observed in previous studies. Lombardini *et al.* [11] and Tritschler *et al.* [12] found that the mixedness in their simulations approached 0.85 asymptotically. Mohaghar *et al.* [6] also found an asymptotic value of 0.8 for mixedness in their experimental study. The mixedness of the 2D case is smaller than that of the 3D case with physical transport coefficients at all times. This suggests that fluids are less molecularly mixed in the 2D configuration. The difference in mixedness between the 2D and 3D cases becomes larger after re-shock, which is probably due to lack of turbulence to enhance mixing in the 2D case.

Mixing can be further studied through the spatial profiles of mole fraction variance. Smaller variance indicates a larger extent of molecular mixing, as the fluid regions are more homogeneous. In fact, mixedness can be related to

the spatial profile of mole fraction variance, by rewriting equation (28) as:

$$\Theta = 1 - 4 \frac{\int \overline{X_{SF_6}^2} dx}{W} = 1 - 4 \int \overline{X_{SF_6}^2} dx^*. \quad (45)$$

Figure 17 shows the profiles of SF₆ mole fraction variance, $\overline{X_{SF_6}^2}$, across the normalized position x^* from the 2D and 3D simulations with physical transport coefficients at different times. All profiles have peaks on the heavier fluid side, which indicates that fluids mix more slowly on the heavier fluid side for this variable-density flow. Similar asymmetries were also observed in other flows with strong variable-density effects [33–35], where they were associated with different inertia of the light and heavy fluid regions. Comparing 2D and 3D profiles at different times, the profile peaks are always larger in the 2D case and this is consistent with the smaller mixedness values for the 2D case. After re-shock, the profiles become more self-similar for both 2D and 3D cases at late times, consistent with the mixedness approaching asymptotic limits. This also suggests that a balanced state between entrainment of pure fluids at the edges of mixing layer and molecular mixing is approximately obtained in both configurations at late times. A similar balanced state was observed in freely decaying variable-density turbulence starting from isotropic turbulent fields by Movahed and Johnsen [36].

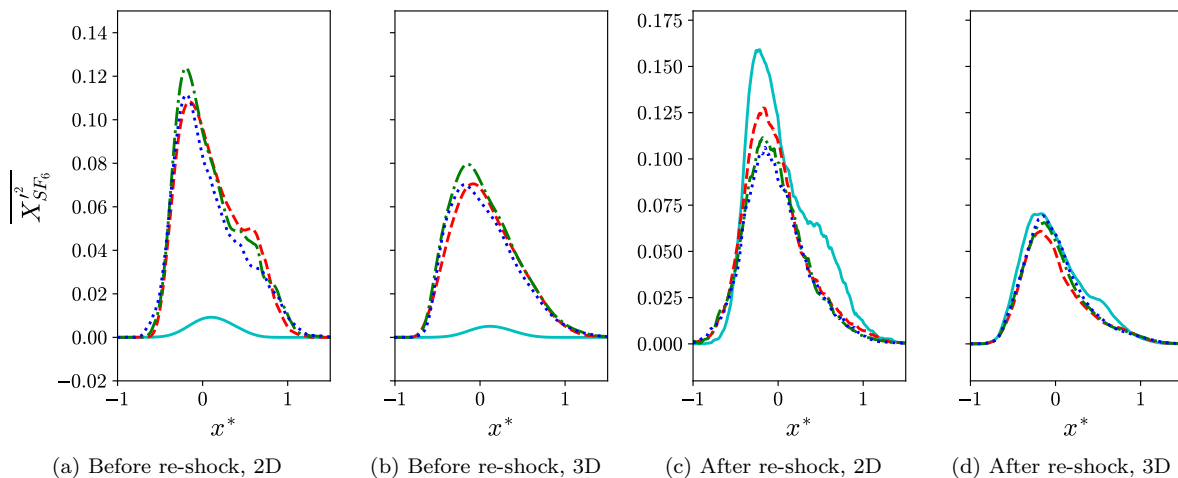


FIG. 17. Profiles of SF₆ mole fraction variance, $\overline{X_{SF_6}^2}$, at different times for the 2D and 3D problems with physical transport coefficients. Before re-shock: $t^* = 0.91$ (cyan solid line); $t^* = 7.25$ (red dashed line); $t^* = 13.6$ (green dash-dotted line); $t^* = 19.9$ (blue dotted line). After re-shock: $t^* = 21.8$ (cyan solid line); $t^* = 25.4$ (red dashed line); $t^* = 29.0$ (green dash-dotted line); $t^* = 31.7$ (blue dotted line).

E. Probability density functions of mole fraction

The discrete probability density function (PDF) of a quantity ϕ bounded by ϕ_{\min} and ϕ_{\max} for the k th bin, where $k \in [1, 2, \dots, N_b]$, can be computed with:

$$\text{PDF} = \frac{N_k}{\Delta\phi N}, \quad (46)$$

where N and N_k are the total number of cells and the number of cells for the k th bin in the central part of mixing layer respectively. $\Delta\phi$ is given by:

$$\Delta\phi = \frac{\phi_{\max} - \phi_{\min}}{N_b}, \quad (47)$$

where N_b is the total number of bins.

The PDF's of SF₆ mole fraction at different times for 2D and 3D cases are compared in figure 18 before re-shock and figure 19 after re-shock. For the 3D case with physical transport coefficients, it can be seen that the PDF has a

quasi-Gaussian shape immediately after first shock resulted from the initial smooth profile of the material interface. However, as pure fluids are being entrained into the central part of mixing layer, two peaks at the pure fluid ends appear. As the instability evolves and the molecular effects start dominating the entrainment, the amplitude of each peak diminishes. With increased transport coefficients or reduced Reynolds number, the peaks at the pure fluid ends can no longer be clearly observed at late times after first shock. The evolution of the PDF for the 2D case is very similar to that for the 3D case with physical transport coefficients, but there seems to be more entrainment over time and the molecular diffusion effect is smaller. This is consistent with previous results that fluids in the 2D configuration are less mixed than those in 3D configuration before re-shock.

After re-shock, there is a common fundamental change in each mole fraction PDF. For each case, the PDF returns to a unimodal shape in the central region of X_{SF_6} values; however, this shape is strongly asymmetric, with the peak in the light fluid region and elongated tail in the heavy fluid region. Moreover, shortly after re-shock, each PDF has two additional peaks near the two pure fluid values. At later times, only the heavy fluid peak ($X_{\text{SF}_6} \sim 1$) survives. The same form was also noticed for the density PDF of Hill *et al.* [9] and mass fraction PDF of Tritschler *et al.* [12] from 3D simulations. The similar shape of the PDF's indicates that each flow is composed of moderately mixed regions of lighter than average fluid and some pure regions of heavier fluid. At later times, the pure light fluid regions are significantly reduced but significant pure heavy fluid regions are still present. The same effect was also observed in other variable-density flows, such as homogeneous RTI by Livescu and Ristorcelli [34], classical RTI by Livescu *et al.* [32, 33], variable-density round jet of Gerashchenko and Prestridge [37], and variable-density shock-turbulence interaction by Tian *et al.* [35]. The central peak of the PDF shifts even more towards the lighter fluid side with smaller Reynolds number, which could be attributed to smaller baroclinic torque generated from smaller perturbation amplitude at re-shock. Thus, the subsequent reduced stirring makes it more difficult for the higher inertia and heavier fluid to mix.

F. Turbulent kinetic energy and Reynolds stress anisotropy

Figure 20 compares the time evolution of mean TKE in the central part of the mixing layer, $\langle \overline{\text{TKE}} \rangle$, between the 2D and 3D cases. The mean TKE is normalized in each case such that it is equal to one at $t^* = 0$ for better comparison between different cases. From figure 20, it can be seen that after first shock, there is a sudden jump in the TKE value for each case. Comparing the 2D and 3D cases with physical transport coefficients, the mean TKE decays after the jump, with similar rates for both cases until $t^* \approx 3$. At later times, TKE decays at a faster rate for the 3D case. This is likely associated with the presence of the vortex stretching mechanism in 3D domain, which enhances the breakdown of large scale features into smaller scales. After re-shock, the distinction in the decay rates between the 2D and 3D cases is much larger, with an even faster decay rate for the 3D case. At lower Reynolds numbers (i.e. for the cases with increased transport coefficients), TKE decays more rapidly after first shock. However, after re-shock, the decay rates among different 3D cases are very similar. This late time weak dependence of 3D TKE decay rate on Reynolds number may be an evidence for the occurrence of mixing transition.

Figure 21 compares the mean profiles of TKE at different times for the 2D and 3D cases with physical transport coefficients. Before averaging in the homogeneous directions to get the mean profiles, TKE is first normalized as:

$$\text{TKE}^* = \frac{(\text{TKE}) W}{\int \overline{\text{TKE}} dx}. \quad (48)$$

Except at the very early times, the normalized TKE profiles approximately collapse when comparing the profiles at later times after both the first shock and re-shock, with only some small variation in the magnitude of the peak. Before re-shock, TKE peaks on the light fluid side ($x^* > 0$) for both 2D and 3D cases, as mixing is more prominent on this side and this is consistent with the mole fraction variance profiles. The TKE peak in the 2D case is higher than that in the 3D case, which means TKE is more localized towards light fluid side under the 2D configuration. However, after re-shock, the peaks of mean TKE^* for both cases move closer to the mid-line or mid-plane ($x^* = 0$) of the mixing layer and the shapes of the profiles for the 2D and 3D problems look more similar.

Besides TKE, the Favre-averaged Reynolds stress anisotropy tensor, b_{ij} , is another statistical quantity of interest from the velocity field. The 2D and 3D anisotropy tensors, b_{ij}^{2D} and b_{ij}^{3D} , are defined as:

$$b_{ij}^{2D} = \frac{\tilde{R}_{ij}}{\tilde{R}_{kk}} - \frac{1}{2} \delta_{ij}, \quad (49)$$

$$b_{ij}^{3D} = \frac{\tilde{R}_{ij}}{\tilde{R}_{kk}} - \frac{1}{3} \delta_{ij}, \quad (50)$$

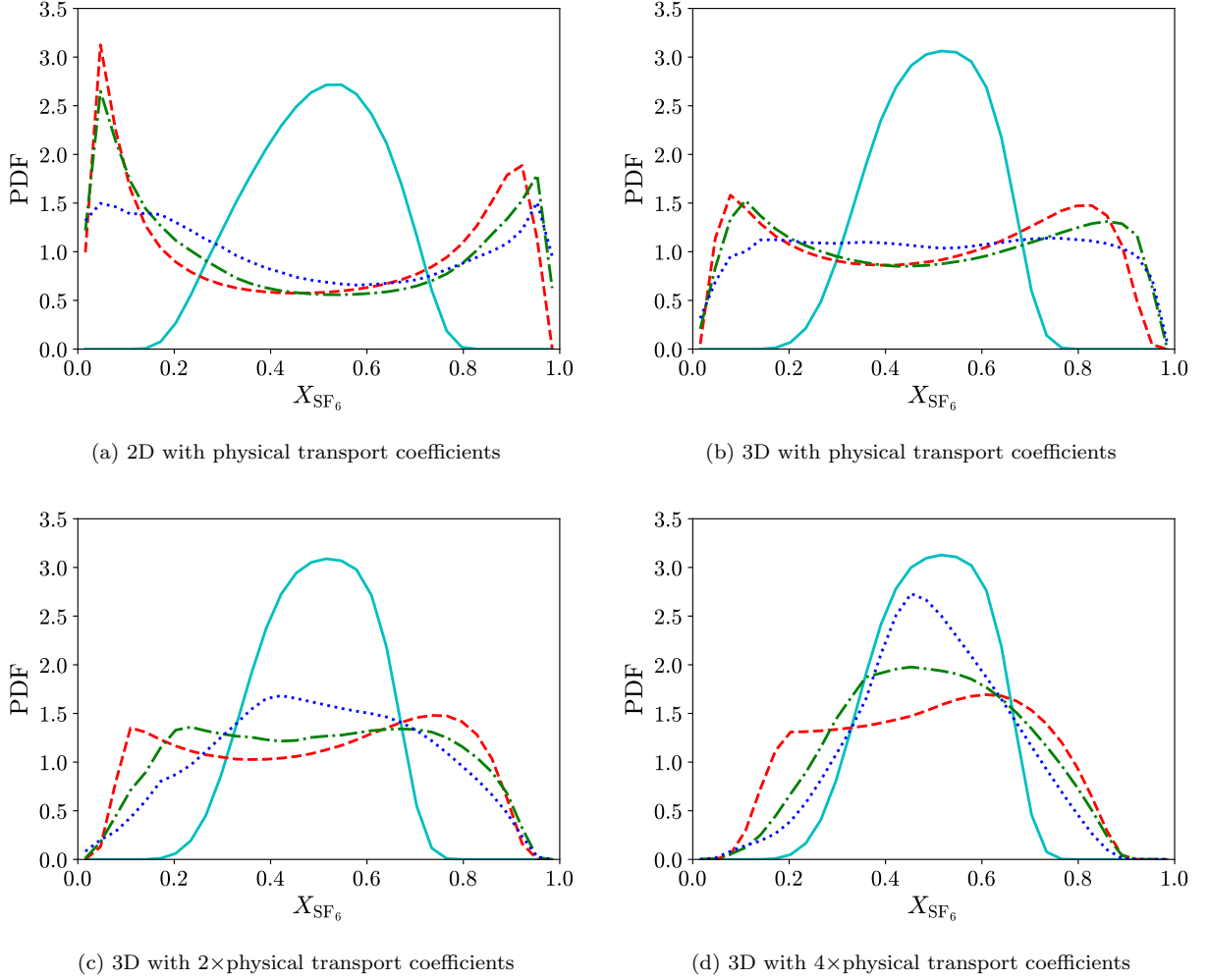


FIG. 18. PDF's of SF₆ mole fraction, X_{SF_6} , for the 2D and 3D problems before re-shock. Cyan solid line: $t^* = 0.91$; red dashed line: $t^* = 7.25$; green dash-dotted line: $t^* = 13.6$; blue dotted line: $t^* = 19.9$.

where δ_{ij} is the Kronecker delta and \tilde{R}_{ij} is the Favre-averaged Reynolds stress tensor given by:

$$\tilde{R}_{ij} = \frac{\overline{\rho u_i'' u_j''}}{\bar{\rho}}. \quad (51)$$

b_{11}^{2D} and b_{11}^{3D} indicate the amount of TKE contributed from the streamwise component of Reynolds normal stresses. $b_{11}^{2D} = 1/2$ and $b_{11}^{3D} = 2/3$ correspond to having all TKE contributed from $\bar{\rho}\tilde{R}_{11}/2$ while $b_{11}^{2D} = -1/2$ and $b_{11}^{3D} = -1/3$ mean that there is no contribution to TKE from that component. The Reynolds normal stresses are isotropic if $b_{11}^{2D} = 0$ in 2D flow or $b_{11}^{3D} = 0$ in 3D flow.

Figure 22 shows the time evolution of mean b_{11} in the central part of mixing layer for the 2D and 3D cases. In all cases, the means of b_{11} almost attain their maximum values of $1/2$ and $2/3$ for the 2D and 3D cases, respectively, right after first shock. This is followed by a reduction of $\langle b_{11} \rangle$ until just before re-shock. However, comparing cases with the physical transport coefficients, $\langle b_{11} \rangle$ decreases more rapidly for the 2D case. Since the kinetic energy decays slower for the 2D case, the faster return to isotropy for this case can be associated with a more efficient TKE redistribution among the Reynolds normal stresses. For quasi-incompressible flows, this redistribution is largely associated with the pressure-strain terms [38] in the Reynolds stress tensor transport equation. Thus, figure 22 implies a stronger pressure-strain correlation for the 2D case as the flow evolves after the interaction with the shock.

At re-shock, there is a sudden decline in $\langle b_{11} \rangle$ values for all cases. For the 2D case, $\langle b_{11} \rangle$ reaches the isotropic value of zero rapidly after re-shock, while for the 3D cases, the TKE fields remain anisotropic until the end of simulations. Comparing the time evolution of $\langle b_{11} \rangle$ among different 3D cases, there is a slightly smaller anisotropy before re-shock

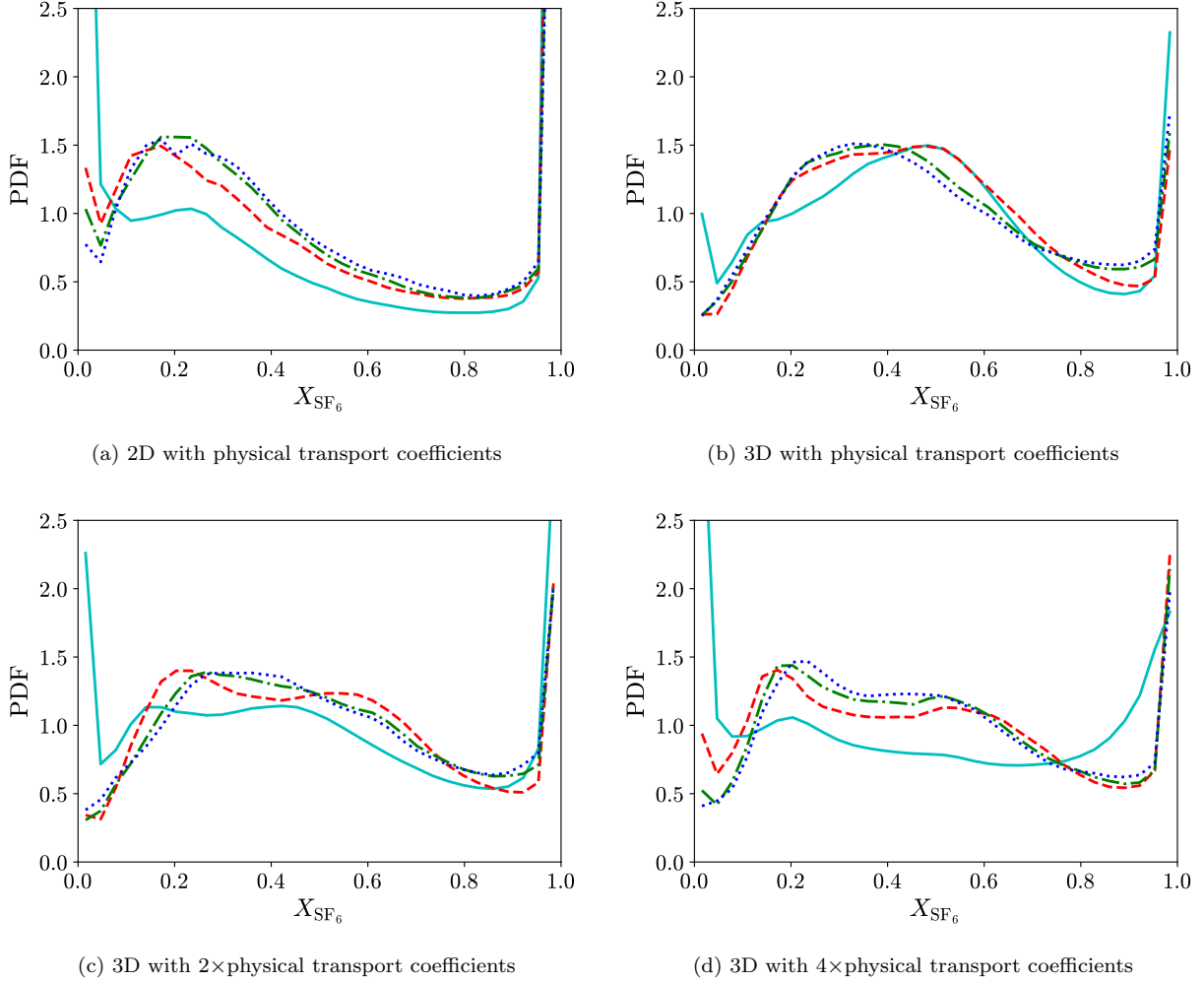


FIG. 19. PDF's of SF_6 mole fraction, X_{SF_6} , for the 2D and 3D problems after re-shock. Cyan solid line: $t^* = 21.8$; red dashed line: $t^* = 25.4$; green dash-dotted line: $t^* = 29.0$; blue dotted line: $t^* = 31.7$.

at lower Reynolds numbers, as diffusive effects are more important at state before the flows become fully turbulent. After re-shock, all 3D cases have similar anisotropy.

Figure 23 compares the mean profiles of b_{11} at different times for the 2D and 3D cases with physical transport coefficients. After first shock, as the flow remains transitional, $\langle b_{11} \rangle$ varies a lot inside the mixing layer for both 2D and 3D cases. However, consistent with figure 22, the overall profile for the 2D case is approaching zero at faster rate. After re-shock, b_{11} has become more uniform inside the mixing layer for both 2D and 3D cases. However, for the 3D case, there is a slight asymmetry between the light and heavy fluid sides, with larger anisotropy on the light fluid side ($x^* > 0$). As seen above, the kinetic energy is larger on the light fluid side, which corresponds to higher Reynolds numbers. Consistent with the time variation of $\langle b_{11} \rangle$, its local values also remain larger at higher Reynolds numbers.

G. Spectra

Figure 24 shows the spectra of SF_6 mole fraction, $\langle E_{X_{\text{SF}_6}} \rangle$, at different times after re-shock computed within the central part of mixing layer for both 2D and 3D cases with physical transport coefficients. At the end time of the simulations, inertial ranges are emerging for both cases. The scaling in the inertial range is close to $\langle E_{X_{\text{SF}_6}} \rangle \propto k^{-5/3}$ for the 2D case and close to $\langle E_{X_{\text{SF}_6}} \rangle \propto k^{-3/2}$ for the 3D case. The scaling of mole fraction spectrum at the end of 3D simulation is close to that of density spectra observed by Tritschler *et al.* [12] in their 3D RMI simulations at early times after re-shock, although long after re-shock they found a smaller gradient scaling for the spectra. Weber *et al.* [39] reported a $-5/3$ scaling for the mole fraction spectra from their 3D RMI experimental results at late times but

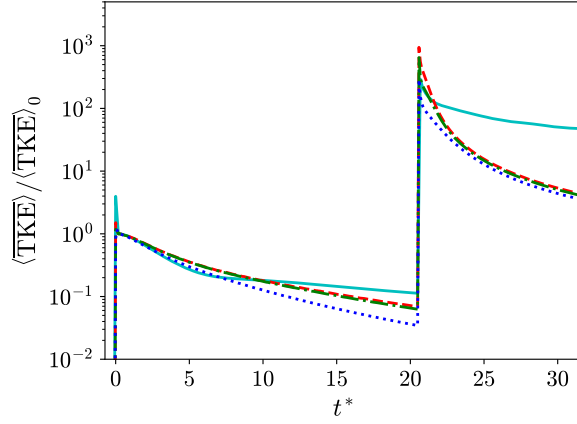


FIG. 20. Comparison of the time evolution of the means of normalized turbulent kinetic energy, TKE, in the central part of mixing layer between the 2D and 3D problems. Mean TKE is normalized by its value at $t^* = 0$, $\langle \text{TKE} \rangle_0$. Cyan solid line: 2D with physical transport coefficients; red dashed line: 3D with physical transport coefficients; green dash-dotted line: 3D with $2\times$ physical transport coefficients; blue dotted line: 3D with $4\times$ physical transport coefficients.

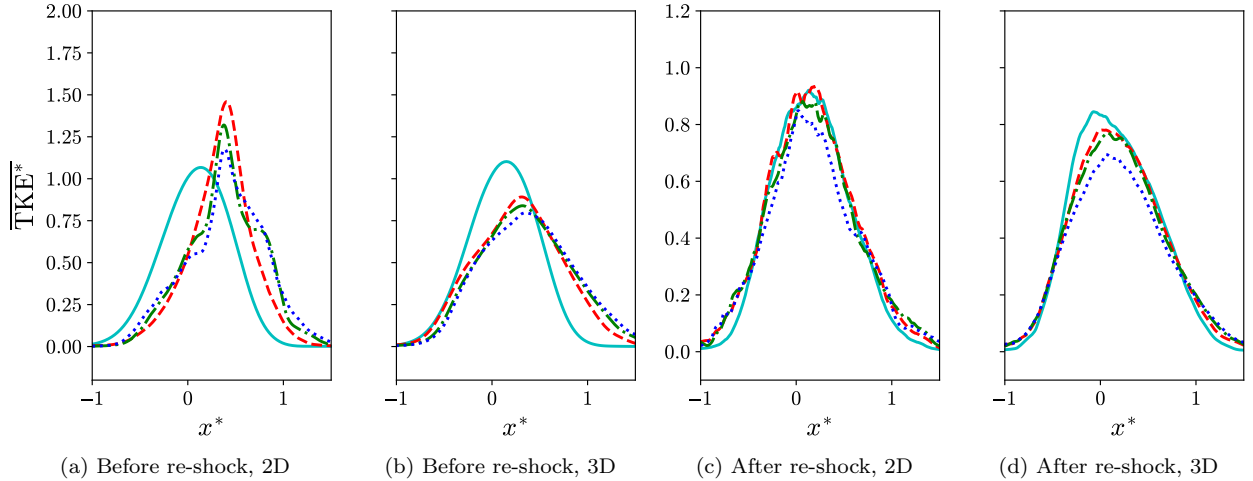


FIG. 21. Profiles of normalized turbulent kinetic energy at different times for the 2D and 3D problems with physical transport coefficients. Before re-shock: $t^* = 0.91$ (cyan solid line); $t^* = 7.25$ (red dashed line); $t^* = 13.6$ (green dash-dotted line); $t^* = 19.9$ (blue dotted line). After re-shock: $t^* = 21.8$ (cyan solid line); $t^* = 25.4$ (red dashed line); $t^* = 29.0$ (green dash-dotted line); $t^* = 31.7$ (blue dotted line).

the experiments did not have re-shock.

To study the energy spectrum in variable-density or compressible turbulence, it is common to decompose the energy as $|\sqrt{\rho}\mathbf{u}|^2$ or $|\sqrt{\rho}\mathbf{u}'|^2$ [34, 40–42]. However, it is pointed out by Zhao and Aluie [43] that one cannot prove spectral locality using energy definitions of the form $|\sqrt{\rho}\mathbf{u}|^2$, because the corresponding transport equations contain terms that are divided by $\sqrt{\rho}$ and can no longer be arranged in divergence form. As a result, viscous effects may not decay at large scales when density variations are large. This lack of locality prevents the corresponding energy to develop an inertial range. Instead, they suggested that kinetic energy defined using Favre (density-weighted) filtering, $\hat{\rho}|\hat{\mathbf{u}}|^2$, where $\hat{\cdot}$ and $\hat{\cdot}$ represent the simple and Favre filtering respectively, can develop an inertial range. While useful for proving locality of energy transfer in the context of filtering, this quantity is not in quadratic form and, thus, not the proper way to form the energy spectrum. The energy spectrum based on $|\rho\mathbf{u}''/\sqrt{\rho}|^2$ energy definition, satisfies the requirement that terms in the corresponding transport equations remain in divergence form, while we still have a quadratic form for the energy [44].

Figure 25 compares the energy spectra computed within the central part of mixing layer with four different energy definitions: (1) $|\sqrt{\rho}\mathbf{u}'|^2$, (2) $|\sqrt{\rho}\mathbf{u}''|^2$, (3) $|\rho\mathbf{u}'/\sqrt{\rho}|^2$, and (4) $|\rho\mathbf{u}''/\sqrt{\rho}|^2$, for both 2D and 3D cases with physical

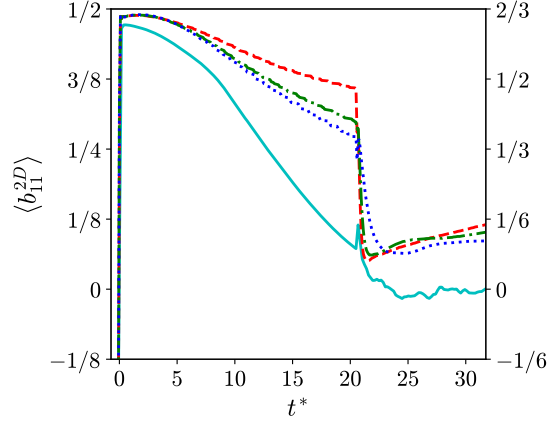


FIG. 22. Comparison of the time evolution of the means of Reynolds stress anisotropy component, $\langle b_{11} \rangle$, in the central part of mixing layer between the 2D and 3D problems. Cyan solid line: 2D with physical transport coefficients; red dashed line: 3D with physical transport coefficients; green dash-dotted line: 3D with $2\times$ physical transport coefficients; blue dotted line: 3D with $4\times$ physical transport coefficients.

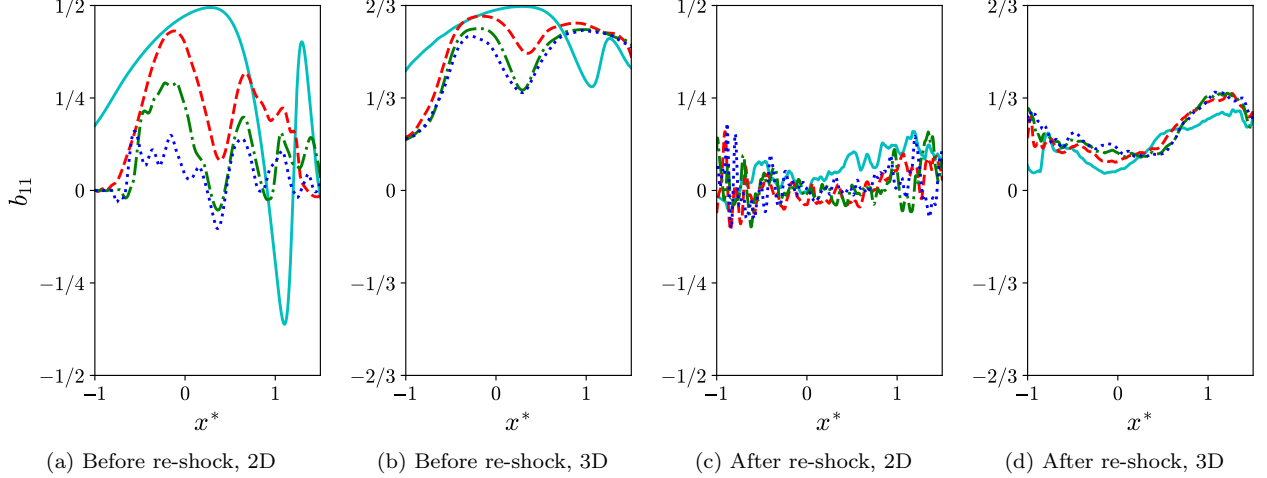


FIG. 23. Profiles of Reynolds stress anisotropy component, b_{11} , at different times for the 2D and 3D problems with physical transport coefficients. Before re-shock: $t^* = 0.91$ (cyan solid line); $t^* = 7.25$ (red dashed line); $t^* = 13.6$ (green dash-dotted line); $t^* = 19.9$ (blue dotted line). After re-shock: $t^* = 21.8$ (cyan solid line); $t^* = 25.4$ (red dashed line); $t^* = 29.0$ (green dash-dotted line); $t^* = 31.7$ (blue dotted line).

transport coefficients, at the end of simulations. Energy definitions using $|\rho\mathbf{u}'/\sqrt{\bar{\rho}}|^2$ and $|\rho\mathbf{u}''/\sqrt{\bar{\rho}}|^2$ yield spectra that are almost indistinguishable for the flow in each case considered here. Also, switching \mathbf{u}' and \mathbf{u}'' has unnoticeable effect on the spectra for other two energy definitions. Although the spectra for the 3D case are close with the choices above, the spectra computed with $|\rho\mathbf{u}'/\sqrt{\bar{\rho}}|^2$ or $|\rho\mathbf{u}''/\sqrt{\bar{\rho}}|^2$ for the 2D case seem to have clearer inertial range than spectra computed with the other two energy definitions, confirming the discussion above.

Figure 26 shows the energy spectra computed with $|\rho\mathbf{u}''/\sqrt{\bar{\rho}}|^2$, $\langle E_{\rho\mathbf{u}''/\sqrt{\bar{\rho}}} \rangle$, at different times for both 2D and 3D cases. As seen from the figure, an inertial range is developing for each case. Comparing the 2D and 3D problems, there is a huge difference in scaling for the spectra in the inertial ranges. The scaling is close to $\langle E_{\rho\mathbf{u}''/\sqrt{\bar{\rho}}} \rangle \propto k^{-2.7}$ for the 2D case but close to $\langle E_{\rho\mathbf{u}''/\sqrt{\bar{\rho}}} \rangle \propto k^{-3/2}$ for the 3D case. Thornber and Zhou [17] found the scaling of spectra of kinetic energy defined as $|\sqrt{\bar{\rho}}\mathbf{u}|^2/2$ close to $E \propto k^{-3}$ at high wavenumbers at late times in their inviscid 2D RMI simulations with different initial perturbations. Similar to our results for the 3D case, Tritschler *et al.* [12] also found scaling of spectra of turbulent kinetic energy defined as $|\sqrt{\bar{\rho}}\mathbf{u}''|^2/2$ close to $-3/2$ scaling after re-shock from their 3D RMI simulations, although the post-re-shock 3D simulation results by Lombardini *et al.* [11] show that a $-5/3$ power law seems to be more appropriate for energy contributed from the streamwise velocity component.

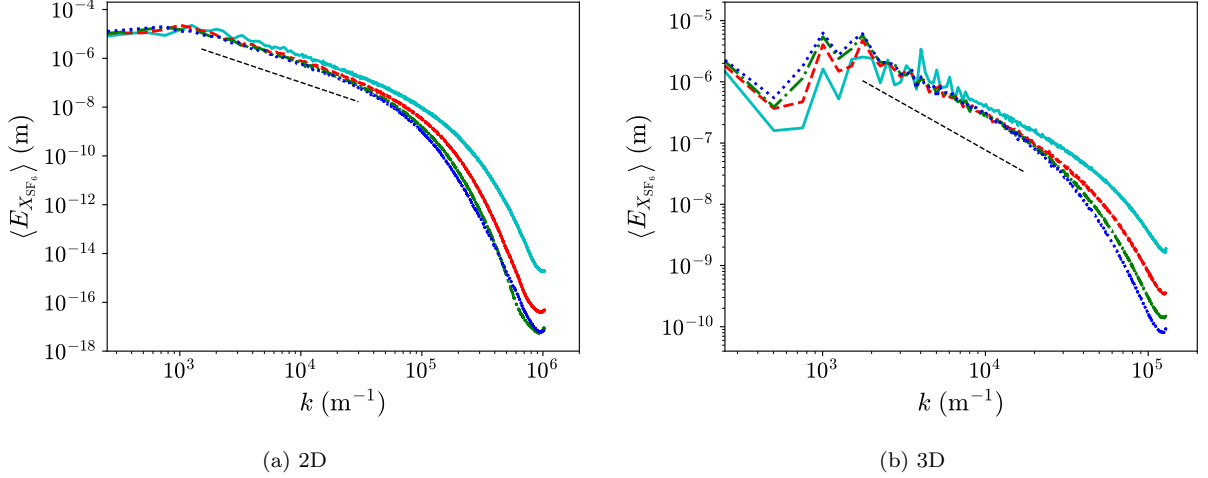


FIG. 24. Spectra of SF_6 mole fraction, X_{SF_6} , at different times after re-shock for the 2D and 3D problems with physical transport coefficients in the central part of mixing layer. Thin black dashed line: $k^{-5/3}/k^{-3/2}$ (2D/3D); cyan solid line: $t^* = 21.8$; red dashed line: $t^* = 25.4$; green dash-dotted line: $t^* = 29.0$; blue dotted line: $t^* = 31.7$.

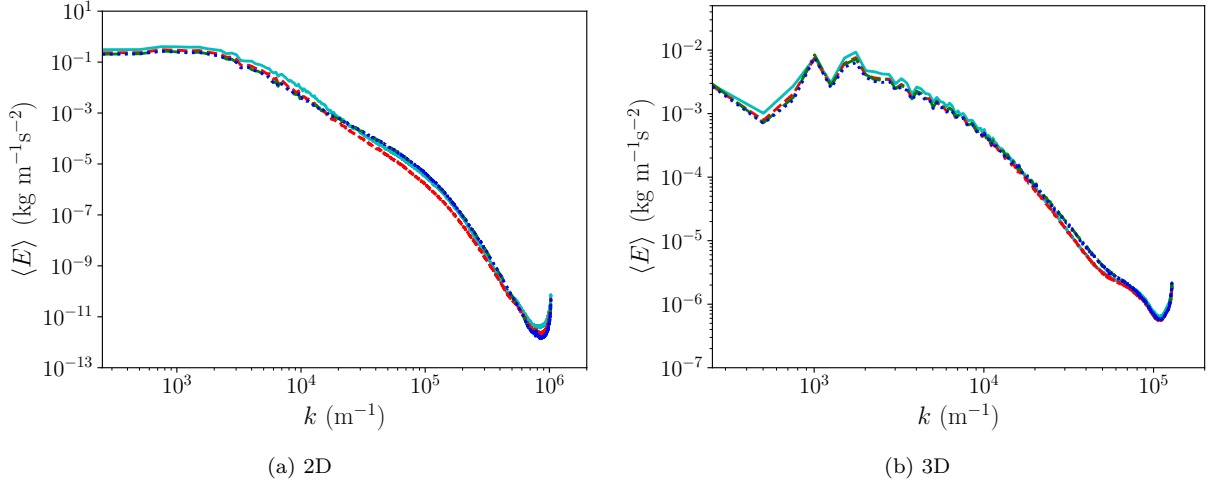


FIG. 25. Energy spectra computed with different energy definitions at the end of simulation ($t^* = 31.7$) for the 2D and 3D problems with physical transport coefficients in the central part of mixing layer. Cyan solid line: $(\sqrt{\rho}u')^2$; red dashed line: $(\sqrt{\rho}u'')^2$; green dash-dotted line: $(\rho u'/\sqrt{\rho})^2$; blue dotted line: $(\rho u''/\sqrt{\rho})^2$.

IX. CONCLUSIONS

We have conducted high-resolution 2D and 3D Navier-Stokes simulations of multi-species mixing driven by RMI. Through grid sensitivity analysis of statistical quantities that are dependent on features of different scales, we have confirmed that the highest grid resolution used for 2D simulations was sufficient to provide accurate statistics that depend on smallest scale features in the flows. Although the highest grid resolution used for 3D simulations is not sufficient to capture statistics that are associated with finest scale features, such as scalar dissipation rate and enstrophy, the grid resolution is high enough for converged statistics that depend on large scale features, such as mixing width and TKE. It was found that, for the chosen initial configuration, the flows inside the mixing layers were only weakly compressible for most of the time under both 2D and 3D configurations. However, the effective Atwood number within the mixing layer remains high throughout the simulations, leading to noticeable variable-density effects. The importance of these effects could be inferred from the asymmetry in the spatial profiles of mole fraction variance and mean TKE, and also the mole fraction PDF's.

The mole fraction profiles become self-similar for both 2D and 3D problems after a short transient regime, following

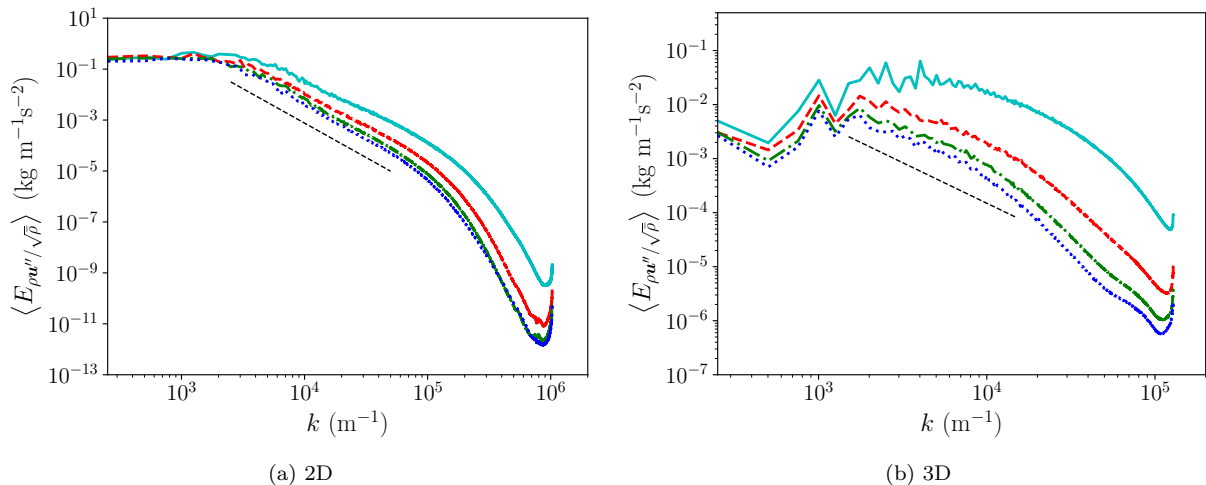


FIG. 26. Energy spectra at different times after re-shock for the 2D and 3D problems with physical transport coefficients in the central part of mixing layer. Thin black dashed line: $k^{-2.7}/k^{-3/2}$ (2D/3D); cyan solid line: $t^* = 21.8$; red dashed line: $t^* = 25.4$; green dash-dotted line: $t^* = 29.0$; blue dotted line: $t^* = 31.7$.

both first shock and re-shock. However, the mixing layer width grows faster for the 2D case after first shock and re-shock. As the mole fraction variance profiles also become more self-similar at late times after re-shock, there appears to be asymptotic but different mixedness values for 2D and 3D problems, where that of the former is smaller. Overall, the temporal evolution of mixedness and PDF of mole fraction at different times indicate that the fluids are more difficult to mix under the 2D configuration than the 3D configuration. We have also compared the time evolution of TKE and anisotropy of the Reynolds normal stresses for both configurations. It is clear that without the effect of vortex stretching to break large scale features into smaller scales, the mean TKE decays slower under the 2D configuration. On the other hand, the Reynolds normal stresses tend to become isotropic at much faster rate after re-shock for the 2D case. The 2D and 3D cases have also been compared by considering the evolution of the mole fraction and energy spectra. There are clearly different scalings in inertial ranges for the 2D and 3D spectra.

The effects of Reynolds number on 3D RMI have also been analyzed by varying the transport coefficients. Through artificially increasing the values of transport coefficients given by diffusivity/viscosity models, the Reynolds number based on mixing width or integral length scale is effectively reduced over time. The effects of reduced Reynolds number are small on the growth of mixing layer width, late-time value of mixedness, and decay rate of TKE after re-shock, but greatly affects the development of many statistical quantities between first shock and re-shock. During this time, the growth rate of mixing layer width decreases, while the decay rate of TKE increases for cases with smaller Reynolds numbers. At the same time, Reynolds normal stresses become isotropic at faster rate with decreased Reynolds numbers. The changes of flow field variables due to Reynolds number effects before the occurrence of mixing transition address the importance of including viscous and diffusive effects in variable-density simulations for accurate predictions of the growth of instabilities.

X. ACKNOWLEDGMENTS

This work was performed under the auspices of U.S. Department of Energy. M. L. Wong and S. K. Lele were supported by Los Alamos National Laboratory, under Grant No. 431679. Los Alamos National Laboratory is operated by Triad National Security, LLC, for the National Nuclear Security Administration of U.S. Department of Energy (Contract No. 89233218CNA000001). Computational resources were provided by the Los Alamos National Laboratory Institutional Computing Program.

Appendix A: Transport coefficients

The shear viscosity, μ_i , of a species i is given by the Chapman-Enskog's model [45]:

$$\mu_i = 2.6693 \times 10^{-6} \frac{\sqrt{M_i T}}{\Omega_{\mu,i} \sigma_i^2}, \quad (\text{A1})$$

where σ_i is the collision diameter and $\Omega_{\mu,i}$ is the collision integral of the species given by:

$$\Omega_{\mu,i} = A (T_i^*)^B + C \exp(DT_i^*) + E \exp(FT_i^*), \quad (\text{A2})$$

where $T_i^* = T/(\epsilon/k)_i$, $A = 1.16145$, $B = -0.14874$, $C = 0.52487$, $D = -0.7732$, $E = 2.16178$, and $F = -2.43787$. $(\epsilon/k)_i$ is the Lennard-Jones energy parameter and M_i is the molecular weight of the species. The values of M_i , $(\epsilon/k)_i$, and σ_i are given in table V.

The bulk viscosity, μ_v , of air is given by the linear model by Gu and Ubachs [46]:

$$\mu_v = A + BT, \quad (\text{A3})$$

where $A = -3.15 \times 10^{-5} \text{ kg m}^{-1}\text{s}^{-1}$ and $B = 1.58 \times 10^{-7} \text{ kg m}^{-1}\text{s}^{-1}\text{K}^{-1}$.

The bulk viscosity, μ_v , of SF₆ is given by the Cramer's model [47]:

$$\mu_v = (\gamma - 1)^2 c_v|_v (p\tau_v), \quad (\text{A4})$$

$$c_v|_v = \left(\frac{c_v}{R} - \frac{f_r + 3}{2} \right), \quad (\text{A5})$$

$$(p\tau_v) = A \exp\left(\frac{B}{T^{1/3}} + \frac{C}{T^{2/3}} \right), \quad (\text{A6})$$

where $f_r = 3$, $A = 0.2064 \times 10^{-5} \text{ kg m}^{-1}\text{s}^{-1}$, $B = 121 \text{ K}^{1/3}$, and $C = -339 \text{ K}^{2/3}$ for SF₆.

The thermal conductivity of species i , κ_i , is defined by:

$$\kappa_i = c_{p,i} \frac{\mu_i}{Pr_i}, \quad (\text{A7})$$

where Pr_i and $c_{p,i}$ are the species-specific Prandtl number and specific heat at constant pressure respectively.

Mass diffusion coefficient of a binary mixture, D_{ij} , is given by [48]:

$$D_{ij} = D_i = D_j = \frac{0.0266}{\Omega_{D,ij}} \frac{T^{3/2}}{p \sqrt{M_{ij} \sigma_{ij}^2}}, \quad (\text{A8})$$

where p and T are the pressure and temperature of the mixture. $\Omega_{D,ij}$ is the collision integral for diffusion given by:

$$\Omega_{D,ij} = A (T_{ij}^*)^B + C \exp(DT_{ij}^*) + E \exp(FT_{ij}^*) + G \exp(HT_{ij}^*), \quad (\text{A9})$$

where $A = 1.06036$, $B = -0.1561$, $C = 0.19300$, $D = -0.47635$, $E = 1.03587$, $F = -1.52996$, $G = 1.76474$, and $H = -3.89411$. M_{ij} , σ_{ij} , and $T_{\epsilon_{ij}}$ are the effective molecular weight, collision diameter, and Lennard-Jones energy parameter respectively for the mixture:

$$M_{ij} = \frac{2}{\frac{1}{M_i} + \frac{1}{M_j}}, \quad (\text{A10})$$

$$\sigma_{ij} = \frac{\sigma_i + \sigma_j}{2}, \quad (\text{A11})$$

$$T_{\epsilon_{ij}} = \sqrt{\left(\frac{\epsilon}{k} \right)_i \left(\frac{\epsilon}{k} \right)_j}. \quad (\text{A12})$$

The values of M_i , $(\epsilon/k)_i$, and σ_i are given in table V.

TABLE V. Fluid properties.

Gas	γ_i	$c_{p,i}$ (J kg ⁻¹ K ⁻¹)	$c_{v,i}$ (J kg ⁻¹ K ⁻¹)	M_i (g mol ⁻¹)	R_i (J kg ⁻¹ K ⁻¹)	$(\epsilon/k)_i$ (K)	σ_i (Å)	Pr_i
SF ₆	1.09312	668.286	611.359	146.055	56.9269	222.1	5.128	0.79
Air	1.39909	1040.50	743.697	28.0135	296.802	78.6	3.711	0.71

Appendix B: Mixing rules

With the assumption that all species are at pressure and temperature equilibria, the ratio of specific heats of the mixture follows as:

$$\gamma = \frac{c_p}{c_v}, \quad c_p = \sum_{i=1}^N Y_i c_{p,i}, \quad c_v = \sum_{i=1}^N Y_i c_{v,i}. \quad (\text{B1})$$

The molecular weight of the mixture is given by:

$$M = \left(\sum_{i=1}^N \frac{Y_i}{M_i} \right)^{-1}. \quad (\text{B2})$$

The mixture shear viscosity, bulk viscosity, and thermal conductivity are given by:

$$\mu = \frac{\sum_{i=1}^N \mu_i Y_i / \sqrt{M_i}}{\sum_{i=1}^N Y_i / \sqrt{M_i}}, \quad (\text{B3})$$

$$\mu_v = \frac{\sum_{i=1}^N \mu_{v,i} Y_i / \sqrt{M_i}}{\sum_{i=1}^N Y_i / \sqrt{M_i}}, \quad (\text{B4})$$

$$\kappa = \frac{\sum_{i=1}^N \kappa_i Y_i / \sqrt{M_i}}{\sum_{i=1}^N Y_i / \sqrt{M_i}}. \quad (\text{B5})$$

-
- [1] R. D. Richtmyer, *Communications on Pure and Applied Mathematics* **13**, 297 (1960).
[2] E. Meshkov, *Fluid Dynamics* **4**, 101 (1969).
[3] S. Balasubramanian, G. Orlicz, K. Prestridge, and B. Balakumar, *Physics of fluids* **24**, 034103 (2012).
[4] B. Balakumar, G. Orlicz, J. Ristorcelli, S. Balasubramanian, K. Prestridge, and C. Tomkins, *Journal of Fluid Mechanics* **696**, 67 (2012).
[5] G. Orlicz, S. Balasubramanian, P. Vorobieff, and K. Prestridge, *Physics of Fluids* **27**, 114102 (2015).
[6] M. Mohaghar, J. Carter, B. Musci, D. Reilly, J. McFarland, and D. Ranjan, *Journal of Fluid Mechanics* **831**, 779 (2017).
[7] D. T. Reese, A. M. Ames, C. D. Noble, J. G. Oakley, D. A. Rothamer, and R. Bonazza, *Journal of Fluid Mechanics* **849**, 541 (2018).
[8] B. Thornber, D. Drikakis, D. Youngs, and R. Williams, *Journal of Fluid Mechanics* **654**, 99 (2010).
[9] D. Hill, C. Pantano, and D. Pullin, *Journal of fluid mechanics* **557**, 29 (2006).
[10] M. Lombardini, D. Hill, D. Pullin, and D. Meiron, *Journal of fluid mechanics* **670**, 439 (2011).
[11] M. Lombardini, D. Pullin, and D. Meiron, *Journal of Fluid Mechanics* **690**, 203 (2012).
[12] V. Tritschler, B. Olson, S. Lele, S. Hickel, X. Hu, and N. A. Adams, *Journal of Fluid Mechanics* **755**, 429 (2014).
[13] A. Subramaniam and S. K. Lele, in *10th International Symposium on Turbulence and Shear Flow Phenomena* (International Symposium on Turbulence and Shear Flow Phenomena, 2017).
[14] M. Lombardini, D. Pullin, and D. Meiron, *Journal of Fluid Mechanics* **748**, 85 (2014).
[15] M. Lombardini, D. Pullin, and D. Meiron, *Journal of Fluid Mechanics* **748**, 113 (2014).
[16] B. J. Olson and J. A. Greenough, *Physics of Fluids* **26**, 101702 (2014).
[17] B. Thornber and Y. Zhou, *Physics of Plasmas* **22**, 032309 (2015).
[18] O. Schilling and M. Latini, *Acta Math. Sci* **30**, 595 (2010).
[19] F. Grinstein, A. Gowardhan, and A. Wachtor, *Physics of Fluids* **23**, 034106 (2011).
[20] J. O. Hirschfelder, C. F. Curtiss, R. B. Bird, and M. G. Mayer, *Molecular theory of gases and liquids*, Vol. 26 (Wiley New York, 1954).
[21] D. Livescu, *Phil. Trans. R. Soc. A* **371**, 20120185 (2013).
[22] F. A. Williams, *Combustion theory* (CRC Press, 2018).

- [23] B. T. Gunney and R. W. Anderson, *Journal of Parallel and Distributed Computing* **89**, 65 (2016).
- [24] B. T. Gunney, A. M. Wissink, and D. A. Hysom, *Journal of Parallel and Distributed Computing* **66**, 1419 (2006).
- [25] R. D. Hornung, A. M. Wissink, and S. R. Kohn, *Engineering with Computers* **22**, 181 (2006).
- [26] R. D. Hornung and S. R. Kohn, *Concurrency and computation: practice and experience* **14**, 347 (2002).
- [27] A. M. Wissink, R. D. Hornung, S. R. Kohn, S. S. Smith, and N. Elliott, in *Supercomputing, ACM/IEEE 2001 Conference* (IEEE, 2001) pp. 22–22.
- [28] M. L. Wong and S. K. Lele, *Journal of Computational Physics* **339**, 179 (2017).
- [29] C.-W. Shu and S. Osher, *Journal of Computational Physics* **83**, 32 (1989).
- [30] M. L. Wong and S. K. Lele, 46th AIAA Fluid Dynamics Conference, AIAA Aviation (2016).
- [31] A. W. Cook, W. Cabot, and P. L. Miller, *Journal of Fluid Mechanics* **511**, 333 (2004).
- [32] D. Livescu, J. Ristorcelli, R. Gore, S. Dean, W. Cabot, and A. Cook, *Journal of Turbulence* , N13 (2009).
- [33] D. Livescu, J. R. Ristorcelli, M. R. Petersen, and R. A. Gore, *Phys. Scr.* **T142**, 014015 (2010).
- [34] D. Livescu and J. Ristorcelli, *Journal of Fluid Mechanics* **605**, 145 (2008).
- [35] Y. Tian, F. Jaber, Z. Li, and D. Livescu, *Journal of Fluid Mechanics* **829**, 551 (2017).
- [36] P. Movahed and E. Johnsen, *Journal of Fluid Mechanics* **772**, 386 (2015).
- [37] S. Gerashchenko and K. Prestridge, *Journal of Turbulence* **16**, 1011 (2015).
- [38] D. Livescu, F. A. Jaber, and C. K. Madnia, *Journal of Fluid Mechanics* **450**, 35 (2002).
- [39] C. R. Weber, N. S. Haehn, J. G. Oakley, D. A. Rothamer, and R. Bonazza, *Journal of Fluid Mechanics* **748**, 457 (2014).
- [40] A. W. Cook and Y. Zhou, *Physical Review E* **66**, 026312 (2002).
- [41] C. Towery, A. Poludnenko, J. Urzay, J. O’Brien, M. Ihme, and P. Hamlington, *Physical Review E* **93**, 053115 (2016).
- [42] P. Grete, B. W. O’Shea, K. Beckwith, W. Schmidt, and A. Christlieb, *Physics of Plasmas* **24**, 092311 (2017).
- [43] D. Zhao and H. Aluie, *Physical Review Fluids* **3**, 054603 (2018).
- [44] D. Aslangil, D. Livescu, and A. Banerjee, under review; LANL Report LA-UR-18-29157 (2018).
- [45] S. Chapman and T. Cowling, *The Mathematical Theory of Non-uniform Gases*, by Sydney Chapman and TG Cowling and Foreword by C. Cercignani, pp. 447. ISBN 052140844X. Cambridge, UK: Cambridge University Press, January 1991. , 447 (1991).
- [46] Z. Gu and W. Ubachs, *The Journal of chemical physics* **141**, 104320 (2014).
- [47] M. Cramer, *Physics of Fluids* (1994-present) **24**, 066102 (2012).
- [48] B. E. Poling, J. M. Prausnitz, O. John Paul, and R. C. Reid, *The properties of gases and liquids*, Vol. 5 (McGraw-Hill New York, 2001).